CHEMISTRY OF MATERIALS

pubs.acs.org/cm

Article

Open Access

This article is licensed under CC-BY 4.0

Fast Li Ion Dynamics in Defect-Rich Nanocrystalline Li_4PS_4I—The Effect of Disorder on Activation Energies and Attempt Frequencies

Anna Jodlbauer,[†] Jonas Spychala,[†] Katharina Hogrefe, Bernhard Gadermaier, and H. Martin R. Wilkening*

Cite This: *Chem. Mater.* 2024, 36, 1648−1664

Read Online

ACCESS | Metrics & More | Article Recommendations | Supporting Information

ABSTRACT: Solid-state electrolytes with fast ionic transport properties will play a crucial role in future energy storage applications that rely on electrochemical reactions. The group of lithium thiophosphates appears to be especially promising as it includes compounds such as $Li_{10}GeP_2S_{12}$, already exceeding the conductivity of conventional liquid electrolytes. Recently, the I-containing thiophosphate, Li_4PS_4I, belonging also to this group attracted great interest due to its theoretically high ionic conductivity that is assumed from the favorable 3D percolation pathways. However, earlier studies showed that ionic conductivity is lower than expected from these structural considerations. Here, we reinvestigated both long-range and short-range ion dynamics through nuclear magnetic resonance (NMR) measurements as well as by conductivity spectroscopy to gain more insights into the conduction mechanism. It turned out that by changing the morphology of Li_4PS_4I, that is, by going from the coarse-grained to the nanocrystalline form, a significant increase in ion dynamics is seen that is accompanied by a change in the Arrhenius prefactor and a clear decrease in activation energy [0.35 eV (nano) and 0.49 eV (micro)] for ionic conduction. We assume that the smaller energy barrier for the nanostructured sample, which was prepared by ball milling, originates form the increased number of defects introduced through mechanical treatment. In line with the reduction in activation energy, we clearly observed an increase in room-temperature conductivity from 2.9×10^{-2} mS cm^{-1} (micro) to 0.47 mS cm^{-1} (nano), that is, by almost two orders of magnitude. Diffusion-induced spin−lattice relaxation ^{7}Li NMR measurements reveal two distinct Li ion diffusion processes. While the slower process shows similar activation energies for both micro- and nanocrystalline Li_4PS_4I, the faster relaxation process displays, however, activation energies of 0.32 and 0.13 eV for the microcrystalline and the nanocrystalline sample, respectively. Additional spin-lock NMR measurements sense long-range ion transport (0.34−0.36 eV) and point to anisotropic ion conduction for both samples. Taken together, the combination of nuclear and non-nuclear methods operating on different time scales help characterize the relevant diffusion pathways in Li_4PS_4I finally leading to the superior behavior of nano-Li_4PS_4I in terms of through-going ionic conduction.

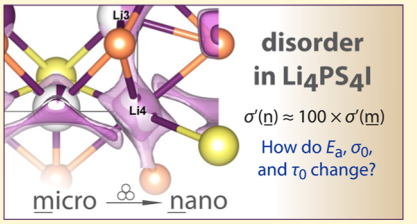

Downloaded via TU GRAZ on May 13, 2024 at 13:05:48 (UTC).
See https://pubs.acs.org/sharingguidelines for options on how to legitimately share published articles.

1. INTRODUCTION

Lithium ion batteries (LIBs) are nowadays considered as one of the key technologies toward more renewable and less polluting energy systems.[1−4] Today, LIBs are already widely used in portable electronics as well as in electric vehicles. Current LIBs rely on liquid electrolytes which pose, however, several safety risks such as risk of leakage and flammability.[5] With the increasing demand for batteries with high energy and higher power densities, the state-of-the-art systems do slowly approach their physicochemical limits. Hence, a new generation of LIBs is urgently needed.[2,6−8]

All-solid-state batteries are considered to have the potential to offer high performance at low cost combined with great safety.[9] This technology requires, however, a highly conducting solid electrolyte material with good electrochemical stability.[10−14] Not only does the conductivity play an important role, but it is also crucial that the ion conductor exhibits favorable mechanical properties, enabling good contact between the electrolyte and the electrochemically active electrode material.[9,15−17]

The group of lithium thiophosphates comprises promising candidates, including compounds such as $Li_{10}GeP_2S_{12}$ (and its derivatives),[18] argyrodite-type materials Li_6PS_5X (X = Br, Cl),[19−22] as well as thio-LISICON-based or Li_2S-P_2S_5 compounds[23−26] that reach room-temperature conductivities of up to 10^{-2} S cm^{-1}. In addition, lithium thiophosphates are usually synthesized at rather low temperatures (<500 °C), which is an advantage compared to oxide based ceramics for which temperatures >1000 °C are needed, which, in addition, can lead to Li loss by vaporization of the precursors.[16,27−29]

Received: November 24, 2023
Revised: December 29, 2023
Accepted: January 2, 2024
Published: January 17, 2024

© 2024 The Authors. Published by American Chemical Society

Nevertheless, these advantages come along with a non-negligible disadvantage, namely, a low electrochemical stability window.[30,31] Fortunately, for $x\mathrm{Li_2S}$-$y\mathrm{P_2S_{5-y}}$LiI, it has been reported that these materials are indeed capable of forming stable interfaces with both electrodes.[32−36]

Earlier studies investigated $\mathrm{Li_2S}$-$\mathrm{P_2S_5}$ compounds with a molar ratio of 2:1 and an addition of 45 mol % LiI. These materials are to be characterized by room-temperature conductivities σ as high as 10^{-3} S cm^{-1}.[37,38] In a more recent study, samples with a composition of $(100 - x)(0.7\mathrm{Li_2S}$-$0.3\mathrm{P_2S_5})\cdot x$LiI were used to study electrochemical stabilities as well as conductivities of glasses and glass ceramics.[39] For a glass with $x = 20$, Ujiie et al. reported a conductivity of 5.6×10^{-4} S cm^{-1} and a very high electrochemical stability.[39] Furthermore, $\mathrm{Li_2S}$-$\mathrm{P_2S_5}$ samples with compositions of 3:1 containing either 35 or 33 mol % LiI ($\mathrm{Li_7P_2S_8I}$) resulted in materials with high conductivities and promising electrochemical stability windows as well.[40,41]

Hence, these encouraging results make electrolytes based on $x\mathrm{Li_2S}$-$y\mathrm{P_2S_{5-y}}$LiI fascinating candidates for future applications and, therefore, interesting model systems for further research devoted to analyze the microscopic conduction mechanisms. In particular, $\mathrm{Li_4PS_4I}$ attracted significant attention due to its theoretically high conductivity originating from its favorable 3D percolation pathways.[42,43] However, so far, experimental values could not reach the expected range for ionic conductivities.[44]

To shed light on this circumstance, Strauss et al.[44] used neutron diffraction measurements to exactly study the crystal structure of $\mathrm{Li_4PS_4I}$ over a large temperature range. Though they pointed out that the Li ion site occupation factors change from ambient conditions down to 10 K,[44] no polymorphic phase transition seems to occur between 295 and 1010 K that may help in explaining the discrepancy between the measured and expected transport properties.

Though structural details are already well explored, apart from a first study by Sedlmaier et al.,[42] a more profound investigation tackling the problem to describe ion dynamics on a wide time scale is not yet available in the literature. While Miß et al.[45] found indications for fast ion dynamics in disordered nm-sized $\mathrm{Li_4PS_4I}$ particles that were embedded in a mixture of different phases, pure nanocrystalline $\mathrm{Li_4PS_4I}$, prepared by a top-down synthesis approach such as ball milling (Figure 1), has not yet been the subject of a larger study. Sedlmaier et al. used a $\mathrm{Li_4PS_4I}$ sample from a solvent-based approach to characterize ion dynamics by means of impedance spectroscopy and static ^{7}Li NMR spin−lattice relaxation (SLR) measurements.[42] Here, we extended this earlier investigation and employed not only variable-temperature laboratory-frame but also rotating-frame ^{7}Li SLR NMR measurements[46−48] in combination with high-resolution ^{31}P and ^{6}Li magic angle spinning (MAS) experiments[49] to shed light on dynamic features and structural details of $\mathrm{Li_4PS_4I}$ in both its microcrystalline (mc) and nanocrystalline (nc) forms. The latter has also been touched recently by Miß et al.[45] Furthermore, conductivity (and impedance) spectroscopy was used to study long-range ion transport.[50] Most importantly, the room-temperature ionic conductivity of nc $\mathrm{Li_4PS_4I}$ prepared by mechanical treatment in a ball mill, see Figure 1, exceeds that of the mc source material by almost two orders of magnitude. We assume that defect structures in the bulk and interfacial effects, possibly including space charge zones,[51−53] are responsible for this increase. Nuclear magnetic resonance (NMR) and impedance data point to anisotropic Li^+ motions, which could also be rationalized by regarding the crystal structure in more detail. Our complementary methodological approach allowed us to identify reduced activation barriers E_a for nc $\mathrm{Li_4PS_4I}$ that are combined with changes in effective jump frequencies ν_{eff}. The latter does also include the migration entropy ΔS_m as a potentially relevant parameter that might govern the change in transport properties seen when going from mc to nc $\mathrm{Li_4PS_4I}$.

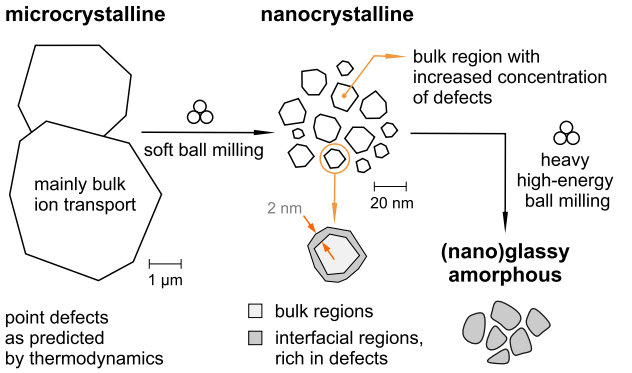

Figure 1. Schematic illustration of the top-down approach that uses ball milling to prepare nanocrystalline ceramics. Harsh milling conditions over a long period will produce amorphous or (nano)-glassy materials. Here, we used a short milling time and a reduced rotational speed to prepare nanocrystalline $\mathrm{Li_4PS_4I}$.

2. EXPERIMENTAL SECTION

2.1. Sample Preparation. For this study, two variants of $\mathrm{Li_4PS_4I}$ were prepared taking advantage of mechanochemical syntheses approaches. Stoichiometric amounts of $\mathrm{Li_2S}$ (Sigma-Aldrich, 99.98%), $\mathrm{P_2S_5}$ (Honeywell Fluka, 99%), and LiI (Sigma-Aldrich, 99.999%) were mixed by hand. Then, the resulting powder was mechanically milled in a high-energy planetary ball mill (Fritsch Pulverisette 7 premium line) at a rotation speed of 250 rpm (rounds per minute) for 2 h (15 min milling, 15 min pause) before increasing both the rotation speed to 450 rpm and the milling time to 40 h (15 min milling, 15 min pause). Milling was carried out in $\mathrm{ZrO_2}$ beakers filled with 180 balls ($\mathrm{ZrO_2}$, 5 mm diameter) and 3 g of overall starting material. Afterward, the mixture was pressed uniaxially into pellets (5 mm diameter) with a pressure of up to 250 MPa. The cold-pressed pellets were fire sealed under vacuum in quartz glass tubes and heat-treated in an oven at 773 K (5 K min^{-1} heating rate) for 24 h. If not stated otherwise, the resulting sample will be called mc one. Parts of this mc sample were again ball milled under rather soft conditions, that is, for only 30 min at 400 rpm, to obtain the nc variant and to reduce the amount of amorphous material as much as possible. All synthesis steps were strictly performed under an inert argon atmosphere (MBraun glovebox with H_2O < 1 ppm, O_2 < 1 ppm) or under vacuum. The starting chemicals were used as received with no special purification procedures.

2.2. X-ray Powder Diffraction. All X-ray diffraction measurements were carried out using a Rigaku Miniflex 600 diffractometer (2θ Bragg−Brentano geometry, Cu Kα) with a D/teX Ultra silicon strip detector. Data were recorded in a 2θ range from 10 to 50° using a step size of 0.02°. The powder samples were protected from contamination with air and moisture by using an airtight sample holder equipped with a Kapton foil window. The diffractograms recorded were analyzed with Malvern Panalytical X'PertHighScorePlus.

2.3. Impedance Spectroscopy. To carry out broadband conductivity measurements, the sample pellets were sputter-coated with Au electrodes (50 nm) on both sides using a Leica EMSCD 050 sputter coater. Impedance measurements were carried out using a NovoControl Concept 80 broadband dielectric spectrometer, cover-

https://doi.org/10.1021/acs.chemmater.3c02988
Chem. Mater. 2024, 36, 1648−1664

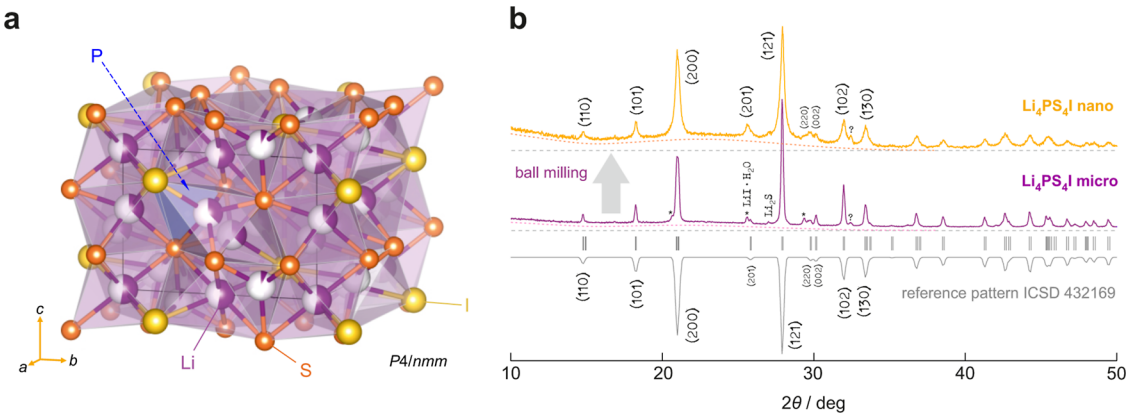

Figure 2. (a) Crystal structure of Li_4PS_4I as determined by high-resolution X-ray diffraction, based on the ICSD reference pattern no. 432169. (b) X-ray powder diffraction patterns of mc (bottom) and nc Li_4PS_4I (top). Nanostructured Li_4PS_4I was prepared by ball milling the mc material that was annealed at high temperatures. Due to the smaller crystallite size in the milled sample, broadening of the reflections is clearly observed. Both patterns reveal rather pure samples mainly differing only in crystallite size; no mechanochemical reactions took place. For comparison, the positions of the reflections of the reference pattern are included as vertical bars. Minor impurities such as $LiI·H_2O$ (asterisks) and traces of Li_2S are indicated, see the text.

ing a range from 10 mHz to 10 MHz and temperatures ranging from 173 to 453 K ± 1 K. The sample temperature was controlled by a QUATRO cryosystem (NovoControl) that uses a stream of freshly evaporated dinitrogen N_2 gas and a heater to automatically adjust the temperature inside the sample chamber with a Eurotherm controller. To prevent sample degradation, an in-house-built airtight sample holder was used. The data were corrected for the resulting (low) cell stray capacitance of this setup.

2.4. NMR Measurements. So-called time domain ^{7}Li NMR measurements were carried out after the powder samples were fire sealed in Duranglass under vacuum. The measurements were performed using a Bruker AVANCE III spectrometer connected to a shimmed cryomagnet with a nominal magnetic field of 7 T. Again a Eurotherm temperature controller was used to vary temperatures between 193 and 503 K with an accuracy of ±2 K. These static, that is, non-MAS NMR measurements were performed using a high-temperature probe (Bruker Biospin) with a ceramic sample chamber. We used both variable-temperature line shape and SLR NMR measurements to collect information on Li^+ jump rates and activation energies. While for the ^{7}Li SLR NMR measurements in the laboratory frame of reference, the classical saturation recovery pulse sequence was employed[54] to monitor the diffusion-induced recovery of longitudinal magnetization $M_z(t)$, for the analogue measurements in the rotating frame of reference, the spin-lock technique was used[54] to measure the transversal decay of the magnetization $M_\rho = M_{(xy)'}(t_{lock})$ in the (xy') plane of the rotating $(')$ coordinate system. The spin-locking frequency was 25 kHz. We used appropriate exponential functions including stretched ones to parametrize the magnetization transients and to extract the SLR NMR rates $1/T_1 \equiv R_1$ and $1/T_{1\rho} \equiv R_{1\rho}$

$$M_{z(\rho)}(t) \propto \exp(-(t/T_{1(\rho)})^{\phi}) \text{ with } 0 < \phi \leq 1 \quad (1)$$

$$M_{z(\rho)}(t) \propto \exp(-((t/T_{1(\rho),1})^{\eta} + (t/T_{1(\rho),2})^{\phi})) + \exp(-(t/T_{1(\rho),1})^{\eta}) \text{ with } 0 < (\eta, \phi) \leq 1 \quad (2)$$

In cases where a single exponential proved insufficient, either a superposition of two exponentials or a function of the latter form was used to analyze the transient curves. In particular, the convolution became necessary at low temperatures when the two exponentials started to overlap.

^{6}Li (73.6 MHz), ^{31}P (202.4 MHz), and ^{127}I (100.1 MHz) MAS NMR spectra were recorded using a Bruker AVANCE spectrometer connected to a shimmed magnet with a nominal field of 11 T, corresponding to a proton Larmor frequency of 500 MHz. The powder samples were pressed into the MAS NMR rotors (2.5 mm in diameter) and kept at a rotation speed of 25(1) kHz during the measurements. The spectra were recorded at slightly elevated temperatures of 303 K. They were recorded with a single pulse 90° sequence and a sufficiently long recycle delay between each scan. Here, we accumulated up to 8000 scans to obtain a satisfactory ^{127}I NMR signal. LiI and 85% H_3PO_4 were used as references to determine the corresponding NMR chemical shifts δ_{iso}. Köcher et al. summarized a number of ^{6}Li chemical shift values; here, if not stated otherwise, we used $\delta_{iso}(^6\text{LiI}) = -3.82$ ppm as our reference value.[55]

3. RESULTS

3.1. Structural Properties. While in Figure 2a the crystal structure of Li_4PS_4I is shown, in Figure 2b, the powder X-ray diffraction patterns of both mc and nc Li_4PS_4I are presented. For comparison, we also included the positions and heights of the reflections of a reference pattern [International Crystal Structure Database (ISCD), no. 432169]. The purity of the coarse-grained sample was verified by Rietveld refinement, which revealed that as-prepared mc Li_4PS_4I is only contaminated with traces of the binary starting materials such as Li_2S, LiI, and $LiI·H_2O$, see also Figure 2b. Small amounts of poorly conducting LiI were also detected by ^{127}I and ^{6}Li MAS NMR, see Figure S1. Rietveld refinement is consistent with a tetragonal lattice ($P4/nmm$) with the lattice parameters $a = b = 8.48$ Å and $c = 5.93$ Å, which is in excellent accordance with results from the literature.[42] Crystalline impurities turn out to be less than 5%.

The structure of Li_4PS_4I consists of PS_4^{3-} tetrahedra forming alternating chains providing up to five crystallographically inequivalent positions for the Li ions. Li(1) and Li(4) are characterized by a 6-fold coordination to four sulfur anions (S^{2-}) in plane and two iodine anions (I^-) in the axial direction. A 4-fold (3S + 1I) and 5-fold (4S + 1I) coordination is observed for the ions residing on the Li(5) and Li(3) positions. Li^+ on Li(2) is tetrahedrally coordinated by two PS_4^{3-} ions each.[42] It has been suggested that Li_4PS_4I provides fast, interconnected 3D diffusion pathways involving all available Li^+ sites. While Li^+ jumping along the c-axis may take place using the regularly occupied Li(3) and Li(4) positions, in-plane hopping is possible via Li(4)−Li(5) exchange processes.[42−44]

https://doi.org/10.1021/acs.chemmater.3c02988
Chem. Mater. 2024, 36, 1648−1664

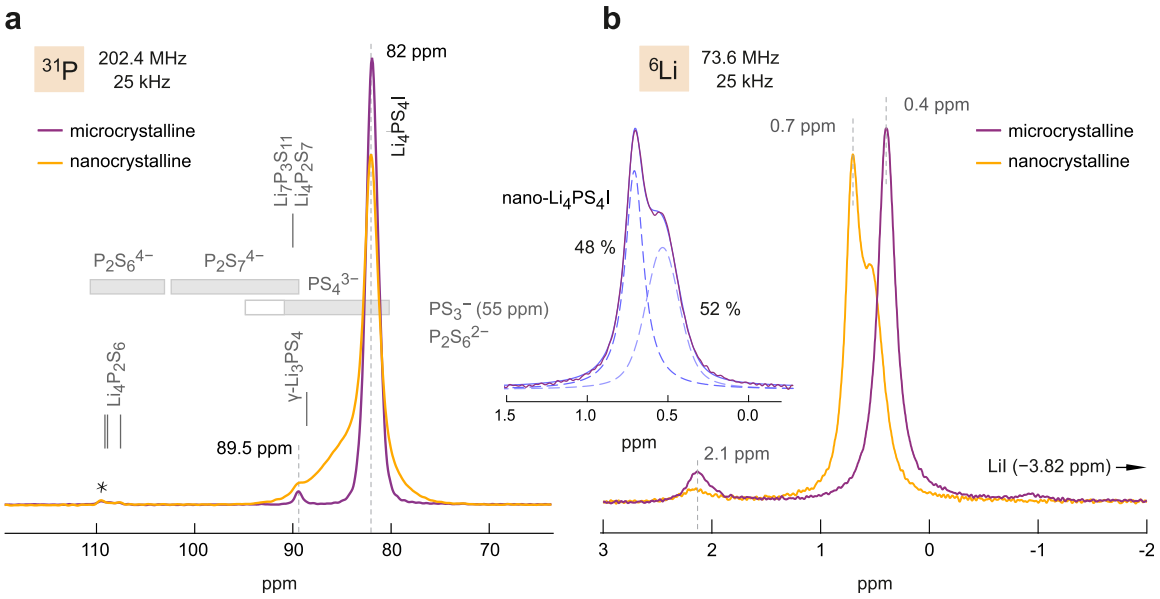

Figure 3. (a) ^{31}P MAS NMR and (b) ^{6}Li MAS NMR spectra for mc and ball-milled (nc) Li_4PS_4I. The NMR spectra were recorded at spinning rates of 25 kHz and at resonance frequencies of 202.4 MHz (^{31}P) and 73.6 MHz (^{6}Li), respectively. Spectra were referenced to H_3PO_4 (0 ppm) and ^{7}LiI (−3.82 ppm vs the chemical shift of solid LiCl); here, we assume no difference in chemical shift between ^{6}Li and ^{7}Li, as the chemical shielding effect should be independent of the magnetogyric ratio. Spinning side bands are marked with asterisks.

Turning to the nc Li_4PS_4I sample, we recognize that the X-ray powder diffractogram shown in Figure 2b is composed of broadened reflections. This broadening is a signature of both small crystallites with mean diameters in the nm range and stress (or strain) introduced during milling. Here, we used the method introduced by Williamson and Hall to estimate the mean diameter of the crystallites and the extent of strain affecting the X-ray results.[56] Since the total width of the reflections is additionally affected by instrumental broadening, we chose the mc Li_4PS_4I sample as a strain-free reference. Due to the long annealing time used to prepare the mc Li_4PS_4I sample, we assume that this sample is mostly unaffected by any strain effects. The final broadening for the nanostructured sample is, therefore, assumed to be only caused by size effects and strain introduced through heavy milling. This first estimation yielded a mean crystallite size $\langle d \rangle$ of approximately 30 nm. We repeated our analysis with a well-defined Li_2S standard and achieved a highly comparable mean crystallite size $\langle d \rangle$ of 22 nm. It turned out that contributions from strain ε take an average value of (5×10^{-3}) that is very similar to that found for other nc ceramics prepared by ball milling.[57,58] The broad hump at low diffraction angles, which is also seen for unmilled Li_4PS_4I, is caused by instrumental effects. The hump at intermediate angles might indicate the formation of an amorphous material. As it is also seen for mc Li_4PS_4I, we cannot rule out that it is due to an instrument effect resulting from our sample holder equipped with Kapton foil, see above.

To collect insights into the structural changes caused by soft ball milling, we used high-resolution ^{31}P MAS NMR and ^{6}Li MAS NMR line shape measurements to study the local magnetic environments at the atomic scale. Figure 3a shows the ^{31}P MAS NMR spectra of the two samples. Microcrystalline Li_4PS_4I displays a sharp line at 82 pm indicating that almost all P atoms experience the same magnetic environment. Comparing the chemical shift δ_{iso} with similar compounds, we notice parallels to Li_3PS_4, especially if we consider the β-variant of Li_3PS_4,[49,59] which displays an almost identical chemical shift range (84−89 ppm)[59] against H_3PO_4. The NMR resonance of ^{31}P in PS_4^{3-} is expected to appear at approximatively 84 ppm.[60] An additional tiny line with an isotropic chemical shift of 89.5 ppm is also seen, which points to another PS_4^{3-} species with a very low occupancy as the area fraction of this feature is below 2% when referenced to the area under the total NMR signal. This tiny NMR line is also seen for nc Li_4PS_4I for which the main signal appears with reduced intensity. It might indicate a small amount of γ-Li_3PS_4, whose chemical shift has been reported to appear at 88.2 ppm with the corresponding ^{7}Li NMR signal at 2.8 ppm.[59] Most importantly, the main ^{31}P MAS NMR line of nano-Li_3PS_4 is asymmetrically broadened, that is, it shows NMR intensities between 82 and 89.5 ppm. Such broadening is diagnostic for a wider distribution of chemical shifts,[61] thus directly visualizing the various local PS_4^{3-} polyhedra distortions. Hence, we conclude that the milling process does not only reduce the crystallite size but also introduces a fair amount of (local) disorder into the system that leads to chemically inequivalent environments for the ^{31}P nuclei. Milling the material for many hours is expected to generate a completely amorphous sample[62] or, in general, nanoglassy materials.[63] It has been reported that amorphous Li_2S-P_2S_5-LiI improves overall ion transport in such systems.[62,64] The fact that, when coming from iodine materials such as Li_4PS_4I, glassy phases have no detrimental influence on ionic transport has also been found theoretically.[43] On the other hand, Miß et al. clearly see an increase in ion dynamics after annealing an amorphous mixture of precursors; they conclude that a disordered nanoscale Li_4PS_4I-related phase is primarily responsible for enhanced ionic conductivity.[45] Here, we expect distorted regions governing the so-called interfacial regions of the nm-sized Li_4PS_4I crystallites, that is, structurally disordered material surrounds the crystallites in the form of a core−shell structure (see Figure 1). Such a heterogeneous structure will provide a network of fast diffusion pathways for the ions. In particular, this network is expected to enhance

https://doi.org/10.1021/acs.chemmater.3c02988
Chem. Mater. 2024, 36, 1648−1664

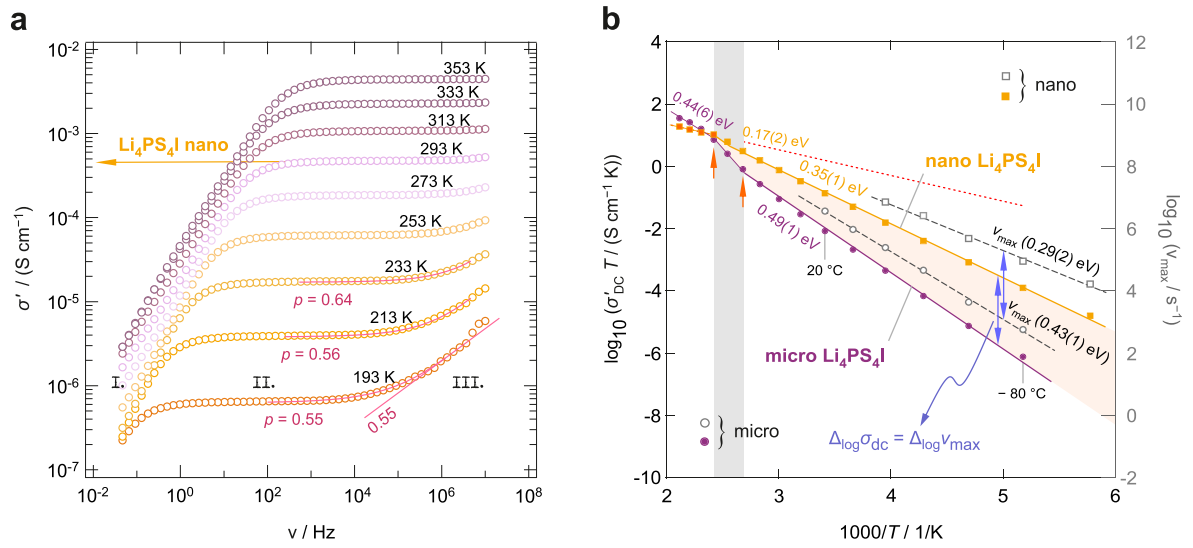

Figure 4. (a) Conductivity isotherms of nc Li_4PS_4I recorded at the temperatures indicated. (b) Arrhenius diagram showing the so-called dc conductivity, plotted as $\sigma_{dc}T$ of mc and nc Li_4PS_4I vs $1/T$. For comparison, the characteristic electrical relaxation frequencies, ν_{max}, deduced from the modulus peaks $M''(\nu)$ are also shown. Values in eV represent the activation energies as obtained from the linear fits (solid and dashed lines). Interestingly, a discontinuity is seen for the Arrhenius behavior at $T \approx 400$ K, which is most pronounced for the ball-milled sample.

even long-range ionic conductivity as is indeed probed here, see the discussion below.

Our ^{31}P MAS NMR lines do not point to huge amounts of amorphous material rather than to local strain, stress, distortions introduced when keeping the milling time as short as possible to generate a sample with nm-sized crystallites. Distortions and even point defects are expected to not only determine the interfacial regions of the nanocrystallites but also to be present in the nm-sized crystalline bulk regions of Li_4PS_4I prepared by ball milling. We estimate that, depending on the deconvolution procedure, approximately 35−50% of the P spins are exposed to these distortions, as is indicated through the broad foot of the ^{31}P MAS NMR line of the nc sample. For comparison, such a broad distribution of resonance lines has also been observed for glassy $Li_7P_3S_{11}$.[65] We believe, however, that huge amounts of completely amorphous material seem to be absent as we would expect not only a much broader ^{31}P MAS NMR line but also lines that span a wider ppm scale, as probed by Seino et al.[66] and partly also by Miß et al.[45] For example, while PS_4^{3-} units in a crystalline matrix show NMR resonances around 88 ppm,[67] the polyanions $P_2S_6^{4-}$ and $P_2S_7^{4-}$ will produce lines at 109 and 97 ppm, respectively.[67] The line of PS_3^- is reported to appear at 55 ppm.[26,67] These chemical shifts may vary also as a function of the extent of distortion and disorder.[66] The characteristic chemical shift ranges are roughly indicated in Figure 3a; a short overview is also given elsewhere.[45]

^{6}Li MAS NMR spectra are displayed in Figure 3b, which were referenced to LiI (−3.82 ppm, see above);[55] the same spectra are shown in Figure S1 (Supporting Information) using a different referencing.[68−70] For mc Li_4PS_4I, we observe a relatively sharp line at 0.4 ppm that is, most likely, already influenced by motional narrowing. It is flanked by an additional line of low intensity at approximately 2.1 ppm. The corresponding area fractions are 95:5 in favor of the main line. Again, as these lines do not coalesce under the NMR conditions, they point to two dynamically distinct Li subsets with magnetically different local environments. It could be that the signal at 2.1 ppm represents Li ions that do not take part in the overall dynamic process governing ionic conductivity at temperatures slightly above ambient, see below. Coalescence of the lines might then be expected to occur at higher temperatures. Such a feature would point to heterogeneous dynamics in Li_4PS_4I, see also below. The origin of the very shallow line at around −1.1 ppm remains unknown so far. Most likely, it represents an almost negligible impurity. Traces of LiI, which serve as a reference to determine the chemical shifts, are seen at −3.82 ppm.[55] A ^{6}Li NMR spectrum of Li_4PS_4I with a wider ppm scale is shown in Figure S1, Supporting Information.

For nc Li_4PS_4I, the situation is similar but the lines are broader if compared to the mc counterpart. Additionally, the main NMR resonance experiences a slight shift from 0.4 to 0.7 ppm and reveals a shoulder on the side that is shifted upfield (approximately 0.5 ppm). From a structural point of view, one may think about the following possible scenario to understand this change. We may interpret the shoulder as a signal that reflects the ions in the inner regions of the nc cores, while the line appearing at 0.7 ppm could represent the rapid ions in or near the interfacial regions, which show a larger degree of disorder. A deconvolution with proper Voigt functions, see inset, shows that the area under the sharp line amounts to approximately 48%, which would agree with results from ^{31}P MAS NMR, see above. A dynamically two-component NMR line shape is also seen in static ^{7}Li NMR, see below. Note that ^{127}I MAS NMR reveals a slightly increased amount of (partly X-ray amorphous) poorly conducting LiI, which has been reformed after ball milling, see Figures S1 and S2, Supporting Information.

3.2. Conductivity and Impedance Spectroscopy. We used solid-state broadband conductivity [alternating current (ac) impedance] spectroscopy covering frequencies from 10^{-2} to 10^7 Hz to gain insights into ion dynamics in both the annealed and structurally disordered Li_4PS_4I samples. In Figure 4a, the real part σ' of the complex conductivity is plotted against the frequency ν for the nc sample; the corresponding isotherms for mc Li_4PS_4I are shown in Figure S2 (see Figure S2, Supporting Information). At low frequencies and high

https://doi.org/10.1021/acs.chemmater.3c02988
Chem. Mater. 2024, 36, 1648−1664

temperatures, electrode polarization (EP) (labeled with I. in Figure 4a) affects the isotherms $\sigma'(\nu)$ and manifests as a linear response. Such polarization is caused by charge carrier accumulation near the ion-blocking Au electrodes.

Toward higher frequencies and temperatures below 273 K, the dispersive regimes (III, Figure 4a), characteristic for unsuccessful (localized) jumps, are visible. Commonly, these regions are approximated by using the Jonscher power law, $\sigma' = \sigma_{dc} + A\nu^p$.[71] While A describes the alternating current coefficient, p is the power law exponent that ranges from 0.6 to 0.9 for many 3D ionic conductors.[71] In general, it may help to rationalize the dimensionality of the ion conduction process as Sidebottom remarked that for 1D conduction $p < 0.4$ is expected, whereas 2D conduction should result in $0.4 < p < 0.6$.[72] Here, the isotherms referring to nc Li_4PS_4I are to be characterized by $p \approx 0.55$, i.e., taking values at the lower 3D limit and, thus, possibly pointing to anisotropic charge conduction in our sample. A similar finding has been presented by Hu and co-workers for Li_3PS_4 with incorporated LiBr.[60] NMR spectroscopy, as discussed below, seems to support this view as different activation energies for the high temperature flanks of the $T_1(1/T)$ and $T_{1\rho}(1/T)$ peaks are probed. Such anisotropic character of overall ionic transport would be in contrast to the earlier studies, suggesting a 3D conduction mechanism for ion dynamics in Li_4PS_4I.[42−44]

Between the two limits, that is, between EP and the dispersive regime, the isotherms $\sigma'(\nu)$ pass through a frequency-independent conductivity plateau (II, Figure 4a), whose characteristic conductivity σ_{dc} is here called the dc conductivity, as $\sigma'(\nu \rightarrow 0)$ would be equal to the total conductivity in the absence of any polarization effects. In general, σ_{dc} represents macroscopic, that is, overall electric transport and is influenced by contributions from bulk regions, grain boundaries, or other interfacial processes. For mc Li_4PS_4I, we obtain 2.9×10^{-5} S cm^{-1} at room temperature. This value is increased to 0.47×10^{-3} S cm^{-1}, i.e., by almost 2 orders of magnitude if we mill the sample. The temperature dependence of

$$\sigma_{dc}T = \sigma_0 \cdot \exp(-E_{a,dc}/(k_B T)) \quad (3)$$

k_B denotes the Boltzmann constant, is shown in 4b. Linear fits yield the activation energies $E_{a,dc}$ of 0.49(1) and 0.35(1) eV for the mc and the nc samples, respectively. Mechanical treatment definitely leads to an increase of σ_{dc} and reduces the activation energy by almost 30%. Finally, an enhancement of σ_{dc} by more than two orders of magnitude at the lowest temperature is measured here. For comparison with the unmilled material, recent studies of Strauss et al.[44] point to an activation energy of 0.45 eV; the authors covered, however, a much smaller temperature range to investigate ion transport in their mc Li_4PS_4I sample. Heating a glassy sample $1.5Li_2S{-}0.5P_2S_5{-}LiI$ (0.28 eV) led to an activation energy of 0.48 eV for a sample annealed at 250 °C.[64] In line with the suggestions by Strauss et al.,[62,64] the formation of structurally disordered regions always lead to an enhancement of ionic transport.

Interestingly, we notice that at temperatures higher than 393 K, the Arrhenius lines show a kink-like behavior, see Figure 4b: the original Arrhenius lines seen at lower temperatures pass into linear regimes that are characterized by activation energies $E_{a,dc}$ of 0.44(6) and 0.17(2) eV, respectively. Particularly for the nc sample, we observe a significant decrease of the activation energy in this high-T regime. Such a deviation, which is also seen for the unmilled sample, could arise from phase transitions or changes in the conduction mechanism. As the Arrhenius line belonging to the nc sample is below that of the nanocrystalline one, a drastic change in Arrhenius prefactor is observed here. Stabilizing this high-T behavior down to room temperature would yield conductivity values exceeding σ'(nano) by another order of magnitude, see the dotted line in Figure 4b. As pointed out by Strauss et al.,[44] in situ XRD does not show a polymorphic phase transition of Li_4PS_4I if temperatures from 295 to 1010 K are considered. Hence, we rule out that a rigorous change of the crystal lattice takes place near 400 K, but order−disorder transitions, affecting solely the Li^+ distribution in its substructure, may still serve as an explanation for such a change.

To understand which spatial region is associated with σ_{dc} and to collect more information on the relevant charge transport mechanisms in both Li_4PS_4I samples, Nyquist plots, i.e., complex plane representations, were constructed, see Figure 5. The plots show the imaginary part Z'' of the complex

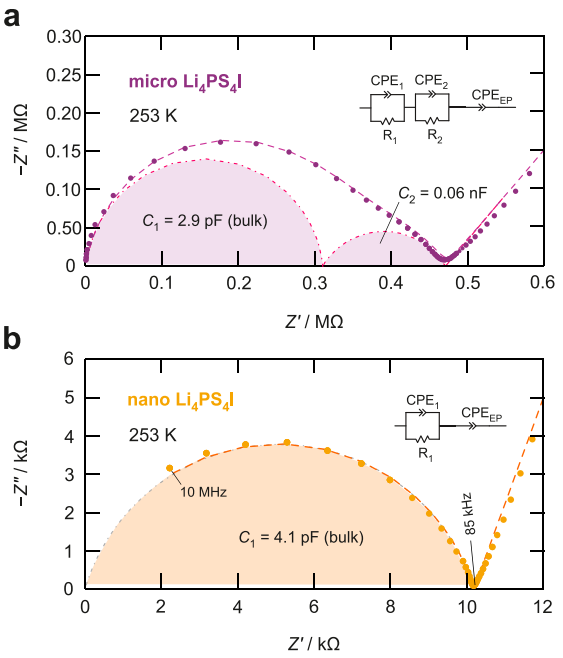

Figure 5. (a,b) Nyquist plots showing the complex impedances $-Z''(Z')$ of mc and nc Li_4PS_4I, respectively. The location curves, which were recorded at 253 K, are approximated with the electrical equivalent circuits shown as insets. Capacitances C_1 of a few pF clearly reveal that the electrical responses reflect intragrain processes. Here, we obtain 2.7×10^{-6} S cm^{-1} for the bulk region and 5.3×10^{-6} S cm^{-1} characterizing total conductivity including interfacial contributions, see the text.

impedance $\hat{Z}$ as a function of its real part Z'. While the circles in these plots represent the data measured at 253 K, the dashed lines show the approximation of the whole location curve with suitable equivalent circuits, see insets. The separate contributions from the bulk and any interfacial regions are indicated by dashed−dotted lines (Figure 5).

In the case of mc Li_4PS_4I, the full equivalent circuit consists of a constant phase element (CPE) taking into account EP and two resistive CPEs (R-CPE), which are needed to satisfactorily parametrize the data. The capacitance for the first depressed semicircle, appearing in the high-frequency regime, was calculated to be C_1 = 2.87 pF, which clearly points to an

https://doi.org/10.1021/acs.chemmater.3c02988
Chem. Mater. 2024, 36, 1648−1664

electrical process (2.7×10^{-6} S cm^{-1}) that is diagnostic for dielectric bulk regions.[73] The second semicircle is associated with a capacitance of C_2 = 0.06 nF (5.3×10^{-6} S cm^{-1}), which could originate from electrolyte−electrolyte interfacial effects or from electrical effects between the electrolyte and the Au electrode. Even another relaxation process in the bulk regions might be associated with this response. Its origin is, however, less clear than that of the semicircle appearing in the high frequency regime. For the ball-milled sample, only a single R-CPE unit combined with a CPE unit for the EP region is needed to reproduce the data very well. The R-CPE unit yields a capacitance of C_1 = 4.08 pF, which indicates that bulk electrical relaxation dominates the response.[73] Hence, three is no doubt that the dc plateaus of the conductivity isotherms shown in Figure 4a represent the electrical intragrain properties of the sample.

To characterize the electrical relaxation processes in the bulk regions of Li_4PS_4I further, we analyzed the corresponding electric modulus data. The imaginary part $M''(\nu)$ of the complex modulus $\hat{M} = 1/\hat{\varepsilon}$, with $\hat{\varepsilon}$ being the (complex) electric permittivity, is shown for nc Li_4PS_4I in Figure 6. Since

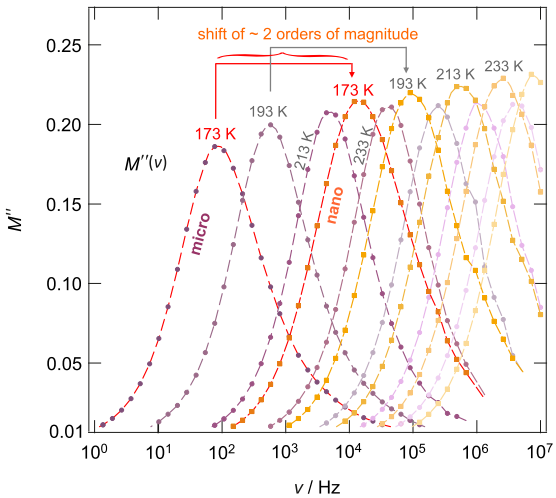

Figure 6. Imaginary part of the electric modulus M'' against frequency ν recorded at temperatures ranging from 173 to 233 K for the mc and the nc Li_4PS_4I samples. Lines are drawn to guide the eye. As compared to the mc sample, the M''(173 K) peak of nc Li_4PS_4I is shifted by two orders of magnitude toward higher frequencies. The corresponding conductivity values σ_{dc} change in the same way, revealing that the increase of σ_{dc} is mainly governed by an increase of the hopping rate when going from mc to nc Li_4PS_4I. The full width at half-maximum of the peaks are 1.5 decades on the frequency axis and, thus, wider than expected for an ideal Debye process (1.14 decades). See the text for further explanations.

the amplitude of M'' is proportional to $1/C$, bulk processes are pronounced in a semilog plot of $M''(\nu)$ vs $\log(\nu/\text{Hz})$. Peak maxima appear at $\nu = \nu_{max}$ with $\nu_{max} \propto \sigma_{dc}$. Hence, the $M''(\nu)$ peaks shift toward higher ν values with increasing temperature. While the $M''(\nu)$ peaks are shown in Figure 6, the resulting electrical relaxation frequencies ν_{max} are analyzed in Figure 4a to directly compare the activation energies $E_{a,M}$ of the two samples with those from conductivity spectroscopy $E_{a,dc}$. In both cases, we find that the activation energies $E_{a,M}$ of the two samples are lower by 0.06 eV (Figure 4b) as compared to $E_{a,dc}$. This difference might be explained by a slight temperature dependence of the effective charge carrier concentration[63]

$$N_c \propto \frac{\sigma_{dc}}{\nu_h} \propto \exp\left(-\frac{E_{a,dc} + E_h}{k_B T}\right) \propto \exp\left(-\frac{E_N}{k_B T}\right) \quad (4)$$

Identifying ν_{max} with the hopping frequency $\nu_h = \nu_{0,e} \exp[-E_h/(k_B T)]$ of the Li ions and using $E_h = E_{a,M}$, since for both mc and nc Li_4PS_4I, the activation energy $E_{a,h}$ is lower by the *same* additive constant of E_N = 0.06 eV, we see that, at any T, the difference of $\sigma'_{dc}T$ and ν_h on the logarithmic scale is $\Delta_{log}\sigma'_{dc}T = \Delta_{log}\nu_h$ (Figure 4b), which yields

$$\frac{\sigma'_{dc,nc}T}{\sigma'_{dc,mc}T} = \frac{\nu_{h,nc}}{\nu_{h,mc}} \text{ and } \frac{\sigma'_{0,nc}T}{\sigma'_{0,mc}T} = \frac{\nu_{0,e,nc}}{\nu_{0,e,mc}} < 1 \quad (5)$$

On the log-scale, we obtain $\Delta_{log}\sigma_0 T = \Delta_{log}\nu_{e,0} = -1.3$, that is, $\nu_{0,e,nc}$ is reduced by a factor of 20 as compared to that of mc Li_4PS_4I. While the effective, or apparent, attempt frequency is given by

$$\nu_{0,e} = \nu_0 \cdot \exp\left(\frac{S_m}{k_B}\right) \quad (6)$$

for the conductivity prefactor, we have to write

$$\sigma_0 = N_0 \frac{e^2 \gamma a^2}{k_B} \exp\left(\frac{S_c}{k_B}\right) \nu_0 \cdot \exp\left(\frac{S_m}{k_B}\right) = b \cdot \nu_0 \cdot \exp\left(\frac{S_m}{k_B}\right) \quad (7)$$

Here, N_0 is the charge carrier concentration at $T \to \infty$, e is the elemental charge, γ is a geometric factor taking into account the dimensionality of the transport process, and a is the jump distance. S_m and S_c denote the entropies of charge carrier migration and formation, respectively. According to eq 5, the change in prefactors, σ_0 and $\nu_{0,e}$, have the same origin, which is given by the product $\nu_0 \exp(S_m/k_B)$. We assume that $\sigma_0/\nu_{0,e} = b$ is the same for the two morphologies of Li_4PS_4I, that is, we do not expect a significant change in jump distance and/or potential charge carrier concentration N_0. Hence, within this simple hopping model either ν_0, S_m or both parameters change when going from mc to nc Li_4PS_4I. Assuming that the difference $\Delta S = S_{m,nc} - S_{m,mc}$ is small, only the change in attempt frequency determines the ratio of the hopping rates. According to Rice and Roth,[74] the attempt frequency, being in the order of Debye frequencies, is, for an ion that is subject to a harmonic potential, given by $\nu_0 \propto \sqrt{2E_h/a^2 m}$, with m being the mass of the particle. A reduction in E_h and/or collective jump processes might indeed lead to a decrease of ν_0. In our case, E_h reduces by 0.14 eV (Figure 4b). Using this value and assuming a group of three ions taking part in the collective jump process would lead to a decrease of ν_0 by a factor of only 2. A rather large number of collectively jumping ions need to be considered to justify a decrease of σ_0 by a factor of 20. It is more likely to assume that in a disordered material, a broader distribution of ν_0 could exist; whether such a distribution has a reduced density at attempt frequencies relevant for the microscopic hopping process remains to be discussed, see below. However, whatever the exact origin is that leads to both a reduction of (i) σ_0 and (ii) the true attempt frequency ν_0 in ball-milled Li_4PS_4I, care has to be taken when interpreting average values from macroscopic measurements with the help of microscopic models. Therefore, we used nuclear spin relaxation measurements (see below) to shed further light on the change of the diffusion parameters.

Before we do so, we will look at the change of the effective prefactor from another perspective. Similar arguments can be

https://doi.org/10.1021/acs.chemmater.3c02988
Chem. Mater. 2024, 36, 1648−1664

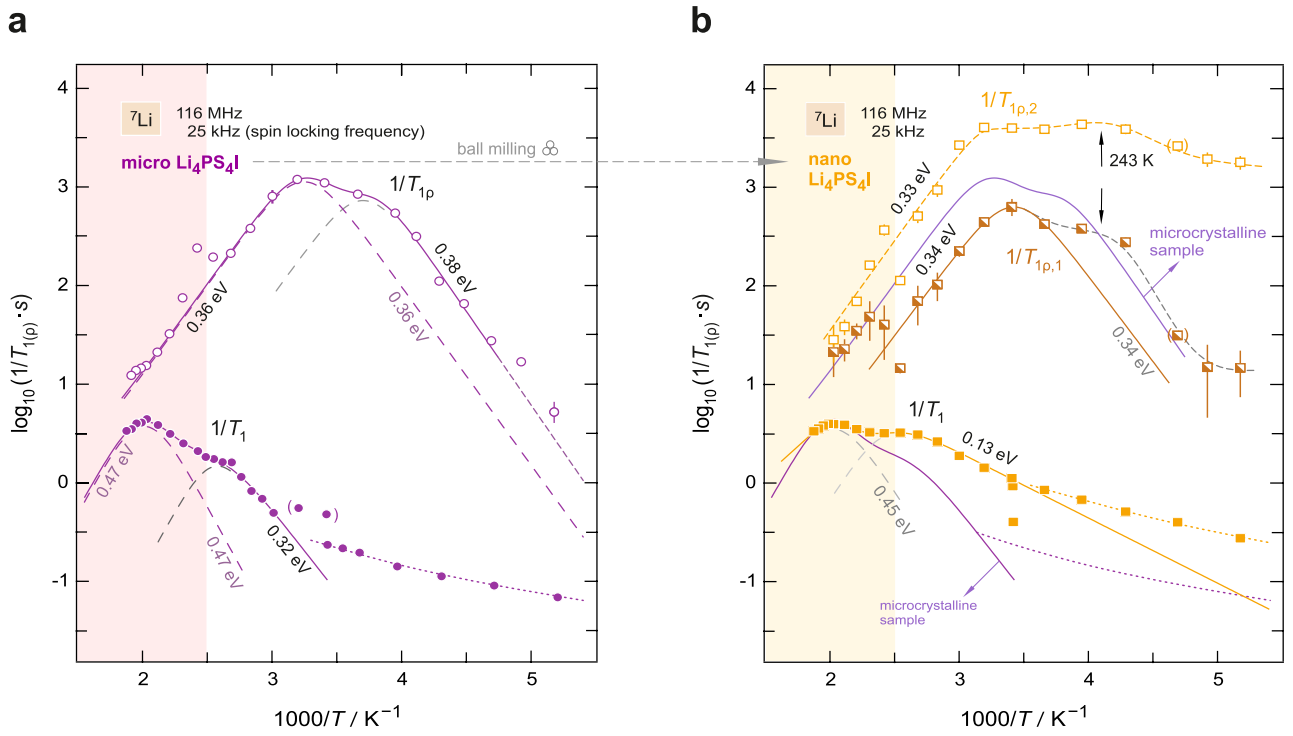

Figure 7. Arrhenius plots showing the temperature dependence of the ^{7}Li NMR SLR rates in the laboratory (R_1) and rotating frame of reference ($R_{1\rho}$) for (a) mc Li_4PS_4I and (b) nc Li_4PS_4I obtained after ball milling. While the relaxation rates were recorded at a resonance frequency of 116 MHz, the spin-lock rates refer to a locking frequency of 25 kHz, which does not take into account any contributions from local magnetic fields. Solid lines show fits according to a BPP-type analysis that uses a combination of two rate peaks to parametrize the whole response. Dashed lines in (a) and in (b) indicate the individual contributions determining the total responses at high T. The dashed line running through the $R_{1\rho,2} \equiv 1/T_{1\rho,2}$ data points is drawn to guide the eye. The same holds for the dotted lines indicating nondiffusive background relaxation seen in $R_1 \propto T^{\kappa}$ NMR at low temperatures. In (b), the location of the curves referring to the mc sample are also indicated.

listed for finding a reduced migration entropy that would also lead to a reduced prefactor. The fact that, in the present case, we obtained $\sigma'_{0,nc}T/\sigma'_{0,mc}T < 1$, is in agreement with the so-called isokinetic rule, colloquially referred to as the Meyer–Neldel rule.[75−77] It predicts that a decrease of E_a will also lead to a decrease of the prefactor $\sigma_0 = f(S_{m,c})$. Such a correlation of the degrees of freedom of the Arrhenius expression could indeed be expected for the same dynamic process, particularly if the measured dynamic range is relatively small. From a historical point of view, this enthalpy–entropy compensation, which is known since 1937, is especially seen for materials with rather high activation energies, i.e., for nonisoentropic processes. However, the rule seems to break down even at too high activation energies. In the present case, the Meyer–Neldel activation energy, Δ_0 in $\sigma_0 \propto \exp(E_{a,dc}/\Delta_0)$ is given by 47 meV, i.e., we have $\Delta_0 > k_BT$ at $T \approx 300$ K. The same value is obtained if we analyze $\nu_h(E_a)$. With $\Delta_0 > k_BT(300\ K)$, Li_4PS_4I still belongs to the so-called type-1 Meyer–Neldel electrolytes.[78] In this class of materials, a reduction of $E_{a,dc}$ significantly increases σ_{dc} at $T \lesssim 300$ K, as is shown in Figure 4b. Here, Δ_0 translates into a rather high isokinetic temperature $T_{iso} = \Delta_0/k_B$ of 1240 K. For comparison, Δ_0 = 47 meV is comparable to that of other Li-bearing phosphates or vanadates[76] but also to garnet-type $Li_6La_3ZrTaO_{12}$ (60 meV)[79] as well as to Δ_0 found in H-bearing amorphous and crystalline Si.[80] Note that in many semiconductors, such as Si, GaAs, and InP, optical-phonon energies range from 36 to 56 meV.[80] Explaining these values quantitatively needs, however, precise information on the coupling mechanisms behind, likely considering the electron–phonon interactions in these materials. In general, for many crystalline alkali ion conductors and glasses, much higher values ranging from 150 to even 200 meV are obtained.[80]

Several attempts, which were undertaken to understand the $\sigma_0(E_a)$ relationship,[75,80] tried to estimate entropy contributions $S_{m,c}/k_B = f(E_h, \tilde{\nu}_0, n)$, with $\tilde{\nu}_0$ and n being characteristic frequencies and number of excitations that are involved in the excitation process. Of course, such a change in entropy caused by a proper statistical consideration of (vibrational) excitation modes could also serve as a valid argument to explain the decrease in the apparent prefactors seen. In the multiexcitation or multiphonon annihilation model of Yelon and Movaghar,[80] the entropy term S/k_B is approximated by $n\ln(N/n) \approx E_h/\varepsilon \ln N$, if $n \ll N$. ε denotes the energy of each phonon quantum and n is the number of phonons that need to be annihilated in the excitation. $N \neq f(E_h)$ represents the number of phonons that lie within the interaction volume, the energy bath, from which they can be annihilated. Within this non-isoentropic approach, which is based on a simple Einstein model of the phonon spectrum, we obtain $\Delta_0 = \varepsilon/\ln N$ that indeed yields the well-known Meyer–Neldel relationship as follows: using $S/k_B = (E_h/\Delta_0)^{\alpha}$ with $\alpha = 1$, we obtain

$$\nu_{0,e} = \nu_0 \exp\left(\frac{S_m}{k_B}\right) = \nu_0 \exp\left[\left(\frac{E_h \ln N}{\varepsilon}\right)^{\alpha}\right] \approx \nu_0 \exp\left(\frac{E_h}{\Delta_0}\right) \tag{8}$$

δ_0 = 47 meV leads to the ratio $\nu_{0,e,mc}/\nu_{0,e,nc} \approx 20$. Here, we obtain $\Delta S_m/k_B \approx 3$, which is in the order of entropies of defect migration.[75] However, the value of ν_0 from this analysis takes a

https://doi.org/10.1021/acs.chemmater.3c02988
Chem. Mater. 2024, 36, 1648−1664

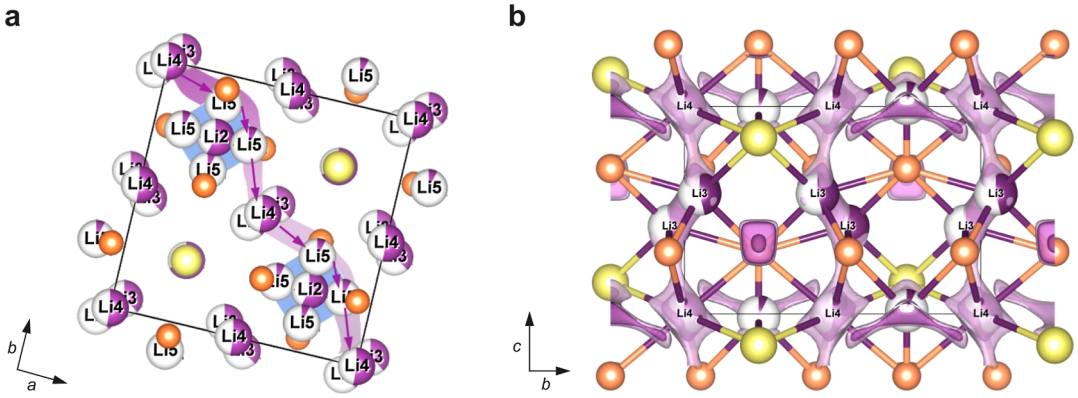

Figure 8. Crystal structure of Li_4PS_4I shown from different perspectives to better visualize the diffusion pathways. (a) Scheme of the possible Li ion pathway along the (110) plane using the Li(4) and the thermally activated Li(5) position. (b) Simulation based on soft bond valence calculations for Li_4PS_4I showing pathways along the Li(3) and Li(4) positions.

value (10^{10} s^{-1}) that is much lower than expected for phonon frequencies. It is also lower than those directly seen by NMR > 10^{12} s^{-1}, see the next section.

In addition, we simply used $\alpha = 1$; in future studies, it might be, however, necessary to correct this general expression by taking into account the exact coupling mechanisms. At least, we found that specific multiexcitation approaches[80] might have indeed the possibility to account for a decrease of the effective attempt frequency by approximately 1.5 orders of magnitude. However, in the special case of ion conductors, we need detailed models to quantify the exact *ion-phonon* coupling that is relevant in solid electrolytes. As announced above, in the next section, we use microscopic experimental methods to work out whether such a decrease in prefactor is seen also with techniques that are sensitive to hopping processes on the angstrom length scale.

3.3. Nuclear Spin Relaxation. *3.3.1. Microcrystalline Li_4PS_4I.* Variable-temperature ^{7}Li SLR NMR measurements, recorded at a Larmor frequency of $\omega_0/2\pi$ = 116 MHz, were used to probe local Li^+ jump processes and their associated activation energies. Figure 7a shows the overall $1/T_1 \equiv R_1$ ^{7}Li NMR relaxation rates of mc Li_4PS_4I together with the corresponding spin-lock rates ($R_{1\rho}$), which will be discussed below.

The data clearly shows a distinct maximum around T_{max} = 500 K with a small shoulder appearing on the low-temperature flank around T_{max} = 380 K. The solid line depicted in Figure 7a represents a superposition of two $R_1(1/T)$ rate peaks following the model according to Bloembergen, Purcell, and Pound (BPP).[81] Hence, NMR, in contrast to electrical measurements, reveals the existence of several dynamic processes in Li_4PS_4I. In the BPP model, the spectral density function $J(\omega_0) \propto R_1$ is given by a Lorentzian-shaped function as it relies on an exponential motional correlation function $G(t')$. Here, we used the BPP equation in a reduced form that only takes into account a single term and excludes a second summand, which considers spin transitions at $2\omega_0$

$$J(\omega_0) \propto \frac{\tau_c}{1 + (\omega_0\tau_c)^\beta} \tag{9}$$

An asymmetry of a given $R_1(1/T)$ NMR rate peak is taken into account by the exponent β for which uncorrelated, isotropic motion yields $\beta = 2$. The (microscopic) activation energy $E_{a,NMR}$ and the Arrhenius prefactor $\tau_{c,0}^{-1}$ are assumed to obey Arrhenius behavior

$$\tau_c^{-1} = \tau_{c,0}^{-1}\exp(-E_{a,NMR}/(k_BT)) \tag{10}$$

It should be noted that the $R_1(1/T)$ NMR rate peak showing up at higher T (see dashed line in Figure 7a) turned out to be fairly symmetric [β = 1.7(7)] with an activation energy of $E_{a,NMR}$ = 0.47 eV. This value is, however, fraught with a large error range as the high-T flank of this peak lies outside the accessible temperature range of our setup. In contrast, the shoulder appearing at lower T displays a significantly lower activation energy of 0.32 eV. Toward even lower temperatures, the data can no longer be described by the BPP model as nondiffusive electronic, paramagnetic (via spin diffusion), and phononic effects start to dominate the relaxation rates.[82−84] These so-called background relaxation rates usually follow a $R_1 \propto T^\kappa$ dependence, with the exponent κ taking characteristic values for, e.g., SLR, purely induced by electronic (κ = 1) or phononic (κ = 2, Raman-type) spin interactions. While pure spin diffusion via flip−flop processes is expected to be temperature-independent (κ = 0), relaxation involving paramagnetic centers turns out to be more complicated as the dependence of $R_1(\omega_0) \propto \omega_0^\beta$ (for $\omega_0\tau_c \gg 1$) depends on whether the polarization transfer is fast or slow and whether it is based on spin diffusion or particle diffusion. If mediated through spin diffusion, a temperature-independent process is again expected in the weaker-than-activated background relaxation regime. Here, for mc Li_4PS_4I, we obtain κ = 2.6(1), which shows that the R_1 rate in this background regime is indeed mainly induced by phononic effects.

The corresponding spin-lock $R_{1\rho}$ rates, which are shown in Figure 7a, do also display two rate peaks as is now expected from R_1 SLR NMR. Each of the $R_{1\rho}$ peaks correspond to one of the R_1 peaks. Our analysis showed that both spin-lock peaks are symmetric in shape ($\beta_{high\text{-}T} \approx 1.7$, $\beta_{low\text{-}T} \approx 2$), yielding very similar activation energies $E_{a,NMR\rho}$ of approximately 0.36 and 0.38 eV, respectively. This suggests that the underlying relaxation mechanisms might differ but need to be characterized by the same energy barriers, which points toward a shared relaxation pathway. The deviation of some of the rates on the high-T flank of peak 1 looks like an additional sharp maximum. Unfortunately, we cannot confirm the existence of such a peak with R_1 measurements as the corresponding temperature T_{max} lies outside the accessible temperature range.

It is worth mentioning that the high-T flanks belonging to $R_1(1/T)$ and $R_{1\rho}(1/T)$ appearing at higher temperatures do not coincide, even for $E_{a,NMR} = E_{a,NMR\rho}$, as it would be expected

https://doi.org/10.1021/acs.chemmater.3c02988
Chem. Mater. 2024, 36, 1648−1664

for a pure 3D (isotropic) ionic conductor. This feature points to an *anisotropic* transport process for which ionic diffusion might be hindered in one direction. Remembering the electrical measurements (see above), this observation is supported by the shape of the conductivity isotherms with their rather low Jonscher exponents also pointing to a nonisotropic, if not low-dimensional, conduction mechanism at sufficiently low T. In Figure 8 possible Li^+ diffusion pathways in the ab-plane and along the c-axis are visualized. Strauss and co-workers mentioned that the occupation of the Li5 site cannot be observed at temperatures as low as 10 K;[44] however, at room temperature, this site becomes thermally activated. Therefore, we suggest that at ambient conditions, the path along the c-axis is energetically favored over the in-plane exchange process, leading to an anisotropic transport characteristic. Soft BV calculations for Li_4PS_4I, see Figure 8b, indeed indicate possible diffusion channels along the Li3 and Li4 positions. However, no clear pathways in the ab-plane could be identified. Hence, the energetically favored hopping path along the c-axis could indeed be the reason for the observed anomalies in both the conductivity experiments and in our NMR measurements.

3.3.2. Nanocrystalline Li_4PS_4I. The R_1 ^{7}Li SLR NMR response of the nc Li_4PS_4I sample is shown in Figure 7b. Again the longitudinal relaxation rates point to two rate peaks. Compared to the unmilled sample, these rate peaks are barely shifted on the temperature scale, that is, T_{max} remains almost the same. However, the peak of nano-Li_4PS_4I appearing at lower T, whose low-T flank is accessible here, shows a greatly reduced activation energy of only 0.13 eV, which points to faster (localized) Li^+ hopping processes in the ball-milled sample as compared to the situation in the unmilled one. The value is comparable with that of Sicolo et al. calculated for ordered Li_4PS_4I.[43] Admittedly, this low-T NMR flank is, however, largely affected by the increased nondiffusive background rates. Here, for nc Li_4PS_4I, background relaxation is ten times higher compared to that in the unmilled phase. Specifically, the NMR background rates of nc and mc Li_4PS_4I run in parallel and differ by a factor of 20, which is very similar to the difference in conductivity prefactors discussed above. The exponent κ describing $R_1 \propto T^{\kappa}$ of the background rates of nc Li_4PS_4I turned out to be clearly larger than 2 [κ = 3.3(2)]. This rather large value shows that additional effects from localized Li^+ diffusion processes seem to be responsible for longitudinal relaxation R_1 in the milled sample and that no pure nondiffusive regime is detected if temperatures down to 180 K are considered, see Figure 7b.

As already touched upon above, the corresponding magnetization transients $M_\rho(t)$ of the spin-lock $R_{1\rho}$ NMR experiments reveal a complex shape leading to the two rates $R_{1\rho,1}$ and $R_{1\rho,2}$ also included in Figure 7b. In some cases, the parametrizing of the transients proved exceedingly difficult; hence, some data points are excluded from our overall Arrhenius analysis and are put in parentheses in Figure 7b. Both the $R_{1\rho,1}(1/T)$ main BPP-type peak and its shoulder, which is also observed for the unmilled sample, are slightly shifted toward lower temperatures (243 K), mirroring, at least qualitatively, faster Li^+ diffusion in Li_4PS_4I. The activation energy, as obtained for the high-T side [0.34(2) eV], is within error limits the same as that obtained from conductivity spectroscopy [0.35(1) eV] on nc Li_4PS_4I. This excellent agreement shows that in the limit $\omega_1\tau_c \ll 1$, spin-lock NMR is able, at least for nc Li_4PS_4I, to probe the same long-range ion transport process as seen by macroscopic electrical measurements. At 243 K, we estimate that the mean jump rate τ^{-1} is in the order of $\tau^{-1} \approx 2\omega_1 \approx 3.1 \times 10^5\ s^{-1}$. This value is by a factor of 10 lower than suggested by ν_{max}, clearly indicating that ν_{max} might be roughly in the order of magnitude of jump rates but has to be, in general, simply regarded as a mean characteristic electrical relaxation frequency.

Turning to the rates labeled $R_{1\rho,2}$, we see that they fairly follow the temperature behavior that is expected for spin−spin rather than for (spin-lock) SLR. There might be a shallow maximum in $R_{1\rho,2}$ at 243 K. However, we would interpret this contribution to the overall $M_\rho(t)$ transients as being influenced by spin−spin interactions rather than being truly affected by spin-lock effects. Importantly and independent of the interpretation of the rates at low T, the flank seen in the high temperature regime is characterized by the same activation energy as found for $R_{1\rho,1}$. The fact that the two rates in this temperature regime do not perfectly coincide does again point to geometrically restricted diffusion in Li_4PS_4I.

3.4. NMR Line Shape Measurements. In addition to diffusion-induced SLR NMR, we probed Li ion dynamics in mc and nc Li_4PS_4I by recording ^{7}Li NMR line shapes, which we obtained at different temperatures by Fourier transformation of the free induction decays after a sufficiently long longitudinal relaxation. In Figure 9 the ^{7}Li NMR lines of mc Li_4PS_4I are presented.

At low temperatures, the overall NMR signal is composed of a quadrupolar powder pattern and a central line. In a first approximation, the main part of the quadrupole pattern, which comprises the 90 and 180° singularities, can be approximated by considering a single axially symmetric electric field gradient as the separation of the outer singularities on the frequency scale is exactly twice that of the inner ones, see Figure 9. In such a case, the distance Δ directly gives the coupling constant C_q = 57.5 kHz. With increasing temperature, this pattern changes. Rapid Li^+ exchange processes cause the pattern to average (see below).[85−87] While at ambient temperature, the original pattern can hardly be seen any longer, a motionally averaged one appears at intermediate temperatures, as will be discussed below. Careful inspection of the quadrupole pattern reveals a further pair of outer satellites, marked in Figure 9 (top) by arrows. Most likely, these (90°) singularities represent another small ensemble of Li spins that is exposed to a much larger field gradient ($C_q \approx 150$ kHz).

Thermally activated Li^+ hopping does also affect the central transition ($\pm 1/2 \leftrightarrows \mp 1/2$). Such line narrowing occurs because of motion-controlled averaging of dipole−dipole interactions to which the spins are subjected in Li_4PS_4I. It is worth noting that the central line does not undergo a homogeneous narrowing process, rather it shows heterogeneous narrowing resulting in the two-component line shape shown in the inset of Figure 9. Heterogeneous line narrowing means that also Li^+ self-diffusion in Li_4PS_4I is of a heterogeneous nature, that is, we have to deal with a distribution of hopping rates instead of a single, averaged motional correlation rate. Such heterogeneous dynamics can easily be traced back to the complex Li^+ substructure presented above. At 253 K, approximately 1/3 of the Li ions are responsible for the narrowed line on top of the broader Gaussian-shaped resonance (see inset of Figure 9) that belongs to the so-called rigid-lattice regime.

The corresponding ^{7}Li NMR line shapes of nc Li_4PS_4I are displayed in Figure 10. While in Figure 10a, the lower part of the spectra is shown, in Figure 10b, the 7Li NMR central lines

https://doi.org/10.1021/acs.chemmater.3c02988
Chem. Mater. 2024, 36, 1648−1664

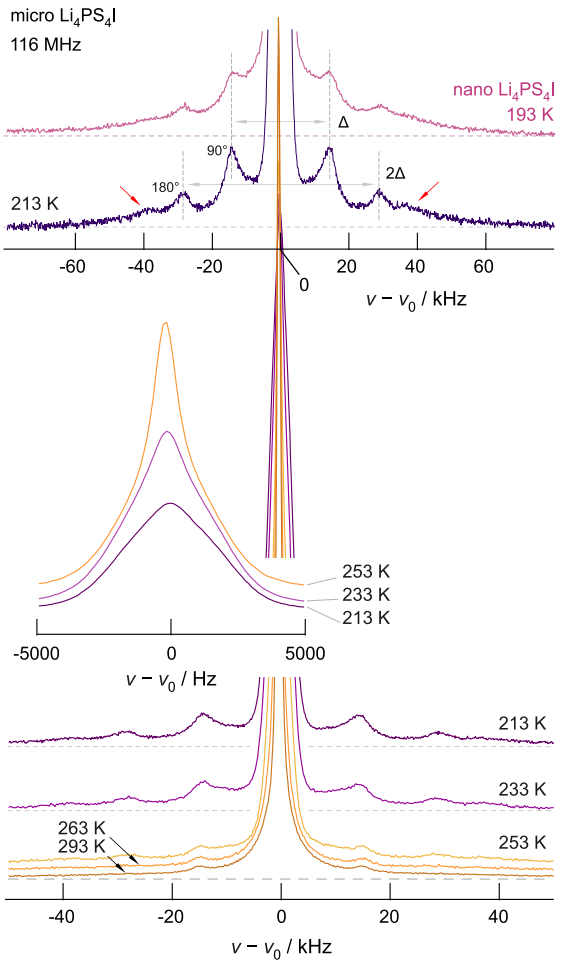

Figure 9. ^{7}Li NMR spectra of mc Li_4PS_4I recorded at the temperatures indicated. While in the lower part, the scaling puts emphasis on the quadrupolar intensities flanking the central transition, the inset shows the heterogeneous narrowing of the central line. In the upper part, a magnification of the quadrupole powder pattern at 213 K is shown. For comparison, the pattern of the ball-milled sample, i.e., nc Li_4PS_4I, is also included. The spectra do almost refer to the rigid-lattice temperature regime. $\Delta = C_q/2$, as indicated, leads to a quadrupole coupling constant of 57.5 kHz that characterizes the main quadrupolar pattern. Arrows point to another set of singularities that is caused by a another small subset of Li ions.

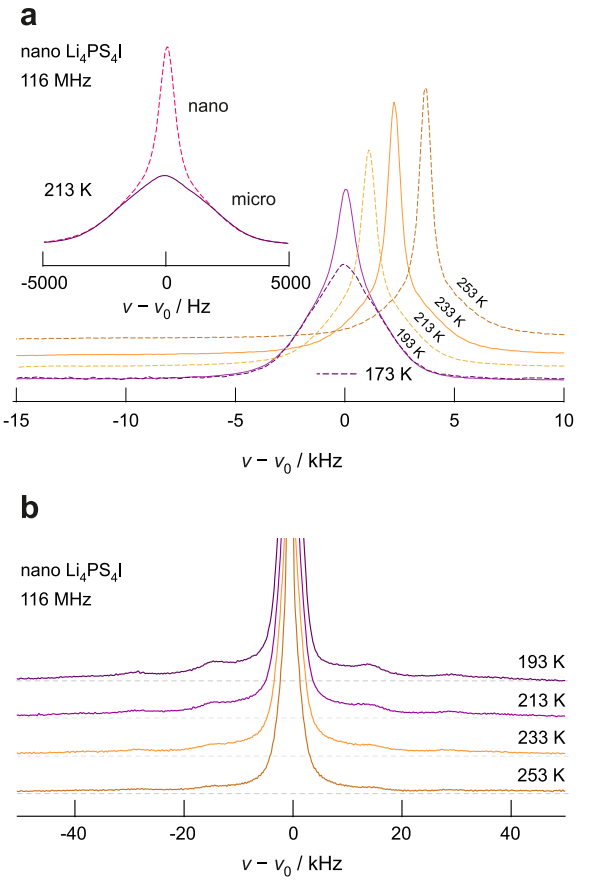

Figure 10. (a) ^{7}Li NMR central lines of nc Li_4PS_4I, which was prepared by ball milling the mc materials; spectra have been recorded at 116 MHz and at the temperatures indicated. In the inset, a comparison of the central lines (213 K) of nc and mc Li_4PS_4I is shown. While the line belonging to unmilled Li_4PS_4I is mainly composed of a single Gaussian line, a two-component line shape is seen after milling; the narrowed line on top of the broad one reflects Li ions being mobile on the kHz time scale defined by the NMR experiment. (b) Magnification of the quadrupole powder pattern of the ^{7}Li NMR lines of nc Li_4PS_4I. At 253 K, we observe that electric quadrupolar interactions are already significantly averaged; this results is in contrast to that obtained for mc Li_4PS_4I, see Figure 9.

are compared that have been recorded at different temperatures.

Again, in the rigid-lattice regime, we clearly detect a quadrupole power pattern, which is, however, less distinct as in the case of the unmilled, fully crystalline sample. Overall, structural disorder and local site disorder sensitively affect the electric field gradients at the nuclear sites and, thus, the overall pattern, as has been observed also for nc $LiTaO_3$ earlier.[88] Whereas for well crystalline samples, patterns with sharp singularities are obtained, for locally disordered samples with their distorted polyhedra, smeared patterns are observed, see the two spectra shown in the upper part of Figure 9. For a completely amorphous sample, a distinct NMR satellite structure would be completely absent, see the discussion on the ^{31}P MAS NMR spectra (vide supra). As in the case of mc Li_4PS_4I, the quadrupole interactions get averaged with increasing temperature. For the ball-milled sample, this process sets in at lower temperatures, corroborating its higher Li^+ diffusivity. While at 253 K the quadrupole pattern of the spectrum belonging to nc Li_4PS_4I is already largely affected by Li^+ hopping, it still reveals a rather clear structure, though reduced in height when compared with that of mc Li_4PS_4I, see Figures 9 and 10b.

Li^+ diffusion also leads to a pronounced motional narrowing for the NMR lines of nc Li_4PS_4I. Again, we observe a two-component line shape, clearly revealing two reservoirs of dynamically distinct Li ions. Generally, in addition to heterogeneous dynamics in the bulk, also the structurally disordered interfacial regions in nc ceramics may constitute another reservoir of fast Li spins, as has also been observed for other nc ceramics.[89−92] Space charge effects might enhance Li^+ diffusion further.[51−53] Likely, the two-component line shape does also lead to the complex decay of the transversal magnetization transients that we acquired in our spin-lock NMR experiments. The existence of effective spin-diffusion effects could serve as an explanation for why the corresponding $1/T_1$ magnetization transients could be parametrized with a single but stretched exponential.

https://doi.org/10.1021/acs.chemmater.3c02988
Chem. Mater. 2024, 36, 1648−1664

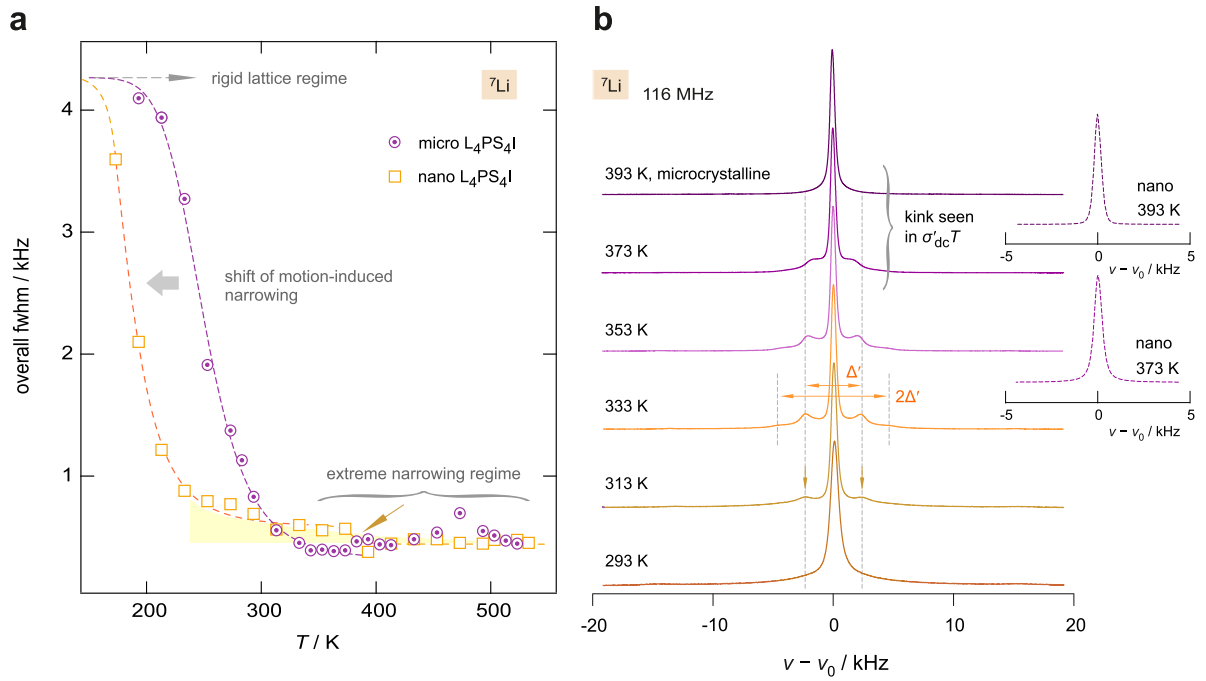

Figure 11. (a) ^{7}Li NMR line width fwhm of mc and nc Li_4PS_4I. The dashed lines represent fits according to the ad hoc model by Hendrickson and Bray. (b) Variable-temperature ^{7}Li NMR lines of mc Li_4PS_4I. Besides the prominent central line of the $\pm 1/2 \leftrightarrows \mp 1/2$ transition, we observe a quadrupole powder pattern $(1/2 \leftrightarrows 3/2)$ emerging when coming from a low temperature and disappearing when going to higher T. See the text for a further discussion of this stepwise activated Li^+ dynamic behavior. The inset shows the NMR resonances of the nanostructured, distorted sample where the distinct satellite intensities are missing.

Most importantly, as compared to mc Li_4PS_4I, heterogeneous narrowing of the lines belonging to nc Li_4PS_4I sets in at much lower temperatures as is illustrated in the inset of Figure 10. This inset compares the NMR lines of mc and nc Li_4PS_4I, which we recorded at 213 K. While for the mc sample, the start of line narrowing can already be divined at this temperature, it is clearly visible for the nc sample. The latter NMR resonance is dominated by the superimposed narrowed line.

In Figure 11, the ^{7}Li NMR line shapes of mc are shown along with those of nc Li_4PS_4I recorded at *higher T*, that is, at temperatures where line narrowing of the central lines is completed. Figure 11 also shows the change of the *overall* fwhm of the central transitions of both samples.

Analyzing the change of the line width in a quantitative way is possibly by approximating the narrowing curve with the help of the model introduced by Hendrickson and Bray, which has, however, originally developed for another purpose.[83] In their model, the NMR line width $\Delta_f \nu(T)$ is given by the following relationship

$$\Delta_f\nu(T) = \Delta_f\nu_0\left[1 + \left(\frac{\Delta_f\nu_0}{B} - 1\right)\exp\left(\frac{E_{a,HB}}{k_BT}\right)\right]^{-1} + \nu_\infty \quad (11)$$

ν_∞ denotes the final width in the extreme narrowing regime, $\Delta\nu_0$ is the width in the rigid lattice regime, E_a, HB represents the activation energy, and B is related to the number of thermally activated spins.[83] Here, activation energies of 0.28(3) and 0.17(2) eV for mc and nc Li_4PS_4I are obtained. We have to note that for both samples, and especially for nc Li_4PS_4I, the narrowing curves are to be regarded as approximations yielding mean values as the lines are actually composed of two contributions. Nevertheless, for nc Li_4PS_4I, the motion-induced curve is clearly shifted toward lower temperatures revealing, at least qualitatively, a significantly higher diffusivity in this sample. It seems that for temperatures higher than 300 K, the line width of this sample continuously decreases slightly further until the extreme narrowing regime is ultimately reached at 400 K. Whether a distinct narrowing step, see arrow in Figure 11a, does exist remains experimentally difficult to confirm. Most likely, this continuous decrease for $\Delta_f \nu(T) < 1$ kHz again reflects a rather wide distribution of jump rates, which is as such not seen for mc Li_4PS_4I.

Importantly, the ^{7}Li NMR line shapes of mc Li_4PS_4I, see Figure 11b, point to a stepwise activation of diffusion processes, and, thus, consecutive activation of Li^+ diffusion pathways in the sulfide. Therefore, the NMR lines support the idea of anisotropic diffusion in Li_4PS_4I as follows: when coming from low temperatures the narrowed central line shows a Lorentzian shape whose lower part is, however, broader than expected. This lower part represents again a dipolarly broadened distribution of another set of electric quadrupolar satellite transitions. The original quadrupolar pattern, see Figure 9, observed at a very low T is averaged such that a residual pattern re-emerges at intermediate temperatures, which is then completely averaged only at higher T, see below. This process is fully reversible. At intermediate temperatures, the pattern is characterized by a single mean quadrupole coupling constant $\overline{C_q} \approx 10$ kHz. At 333 K, the pattern is fully developed and its inner (90°) and outer (180°) singularities, separated by $\Delta = \overline{C_q} \approx 10$ kHz, are best seen, cf. Figure 11b. This characteristic feature resembles the universal behavior of solid-state NMR lines of complex crystalline materials such as other thiophosphates,[54,93] thioborates,[85−87] and silicates.[94]

If the temperature is increased further, the reduced pattern undergoes additional changes (Figure 11b) and is finally

https://doi.org/10.1021/acs.chemmater.3c02988
Chem. Mater. 2024, 36, 1648−1664

completely averaged by Li^+ exchange processes that come into play when T reaches values as high as 360 K. At 393 K, the spectrum is solely composed of a single central line (Figure 11b). Again, according to our study, we deal with a reversible change in line shape. Ion dynamics causing this averaging process proceed on a much longer time scale than those being responsible for motional narrowing of the original quadrupole powder pattern and of the central transition (Figure 11). Note that narrowing of the central line is fully completed at 350 K. Obviously, the already mobile Li ions in Li_4PS_4I get (stepwise) access to further diffusion pathways at temperatures higher than 300 K. This feature supports our idea about nonisotropic self-diffusion of Li^+ in Li_4PS_4I, see above. It might be related to the Li signal appearing at 2.1 ppm, see Figure 3b, which could mirror Li sites that do not participate in overall Li^+ diffusion at ambient conditions but get involved in rapid exchange processes only at higher T.

Another explanation of the stepwise changes seen in NMR electric quadrupolar interactions would be a (reversible) rearrangement of the Li ions in Li_4PS_4I occurring at higher T. In such a scenario, the Li ions would have to occupy sites with no electric field gradients, which is only expected for a highly symmetric electric charge distribution at the nuclear sites. Such a nondynamic scenario is, however, rather unlikely. We believe that the stepwise reversible appearing and disappearing of the quadrupolar powder pattern of mc Li_4PS_4I reflects a *dynamic* feature. It excellently agrees with the deviation of the $\sigma_{dc}'T$ Arrhenius line starting at 370 K and passing into a new Arrhenius line at 400 K, see the arrows and the gray area in Figure 4b. Obviously, this change in conductivity Arrhenius behavior is related to the changes seen in NMR line shape measurements.

Finally, for nc Li_4PS_4I, we do not observe a partly averaged quadrupolar powder pattern re-emerging at intermediate temperatures. The original electric quadrupolar pattern, which is seen only at very low T (Figure 10b), is completely averaged at temperatures above ambient and no new satellites reappear, see the ^{7}Li NMR lines included in Figure 11b on the right. Hence, although overall Li^+ diffusion is without doubt of a heterogeneous nature in nc Li_4PS_4I, as is evidenced by the two-component central line (Figure 10a), the absence of such a clear intermediate quadrupolar powder pattern shows that no large Li subensemble remains immobile on the NMR time scale in the temperature regime of extreme motional narrowing ($T > 300$ K). This finding is in agreement with the significantly reduced intensity of the ^{6}Li MAS NMR line seen at 2.1 ppm, cf. see Figure 3b. In other words, the local distortions introduced through milling ensure that already at temperatures as low as 300 K (see Figure 11), almost all Li ions participate in overall translational dynamics.

3.5. Comparing Results from NMR and Conductivity Measurements. *3.5.1. Longitudinal Relaxation in Li_4PS_4I.* We believe that the two-component ^{7}Li NMR line shapes seen for both samples, but more pronounced for nanostructured Li_4PS_4I at low temperatures, could easily lead to the nonexponential magnetization transients and to several superimposed diffusion-induced NMR rate peaks. Indeed, as has been discussed above, deviations from pure exponential behavior has been observed and the ^{7}Li NMR rates R_1 of unmilled Li_4PS_4I pass through two rate peaks (see Figure 7a). It is worth mentioning that the peak appearing at higher T is located in the temperature regime ($T > 400$ K) where the conductivity Arrhenius lines have already entered a regime with another activation energy, as indicated in Figure 4b. This fact needs to be considered when comparing results from NMR and conductivity data. Here, the prefactors $\tau_{c,0}^{-1}$ of the two rate peaks are as follows: for the high-T peak, we obtain $\tau_{c,0}^{-1} = 8 \times 10^{13}$ s^{-1} and for the peak showing up at lower T, the factor is given by $\tau_{c,0}^{-1} = 2 \times 10^{13}$ s^{-1}. We find that a lower activation energy is combined with a prefactor $\tau_{c,0}^{-1}$ slightly reduced by a factor of 4. As just mentioned, the two rate peaks refer to two different Arrhenius regimes as probed by conductivity spectroscopy and discussed above. Nevertheless, values in this order of magnitude are highly comparable to those commonly expected for (Debye-type) phonon frequencies.

The most striking difference when going to nc Li_4PS_4I is, however, given by the fact that the peak at low T remains unshifted on the $1/T$ scale but is reduced in its low-T activation energy (see Figure 7b). Hence, localized, correlated Li^+ movements are facilitated in nc Li_4PS_4I, which might also trigger long-range ion dynamics as probed by conductivity spectroscopy. Since we have no direct access to the high-T NMR flank, the associated prefactor cannot be properly determined; a rough estimation via the BPP analysis shown in Figure 7b, which leads to 10^{13} s^{-1}.

3.5.2. Spin-Lock Relaxation in Li_4PS_4I. In the case of spin-lock NMR, the rates belong to the lower temperature regime ($T < 400$ K) for which no change in the conductivity Arrhenius line is seen. Additionally, spin-lock NMR is sensitive to a time scale that is more comparable to that probed by (dc) conductivity spectroscopy. The situation for spin-lock NMR is as follows: the two peaks detected for mc Li_4PS_4I (see Figure 7a) are to be characterized by $\tau_{c,0,\rho}^{-1} = 0.2 \times 10^{12}$ s^{-1} (at high temperatures) and $\tau_{c,0,\rho}^{-1} = 6 \times 10^{12}$ s^{-1} (at lower temperatures). These factors differ by a factor of 30 and show a larger prefactor for the peak appearing at lower T as expected for a pair of peaks that shift on the $1/T$ scale but have almost the same high-T activation energies $E_{a,NMR}$ (0.36, 0.38 eV). For the rate peaks of the nc sample (see Figure 7b), we obtain prefactors increased by 20% but with the same ratio of approximately 30. Again, an increase in $\tau_{c,0,\rho}^{-1}$ is seen when a peak with the same shape appears at lower T. Prefactors in the order of 10^{12} s^{-1} are in the lower range of phonon frequencies. For comparison, at least the two Arrhenius lines $\nu_{max}(1/T)$ point to $\nu_e(1/T \rightarrow 0)$ rates being in the same order of magnitude as NMR does. We obtained 1×10^{13} s^{-1} for mc Li_4PS_4I and 2×10^{12} s^{-1} for the nc sample, see Figure 4b. For comparison, recent calculations by Albe and co-workers point to a prefactor in the order of 2 THz for ordered Li_4PS_4I.[43]

Taken together, as compared to the trend that determines the Arrhenius lines of conductivity and electric modulus spectroscopy (cf. the discussion of Figure 4), the opposite change in prefactors is seen by atomic-scale spin-lock NMR. Here, the shift of the diffusion-induced rate peaks in spin-lock NMR does lead to a slight increase of $\tau_{c,0,\rho}^{-1}$ rather than to a decrease. If we assume that $\tau_{c,0}^{-1}$ of NMR is a true attempt frequency rather than an effective or apparent one, the change in σ_0 and $\nu_{0,e}$ has to be looked for in a change of the overall entropy rather than in a shift of the characteristic frequencies of the modes to which the jumping ion is subjected. To conclude, while we definitely see a Meyer−Neldel change in prefactors when studying macroscopic dc conductivity data in the T regime below 400 K, a reduction in attempt frequency by atomic-scale methods, such as spin-lock NMR, can hardly been recognized. In contrast, in the case of Li_4PS_4I, we observe even

https://doi.org/10.1021/acs.chemmater.3c02988
Chem. Mater. 2024, 36, 1648−1664

a slight increase in attempt frequency rather than a decrease. As a last remark, if we assume that the above-mentioned ratio of 30 is related to the change in (effective) attempt frequency, electric relaxation in mc Li_4PS_4I could be primarily influenced by the spin-fluctuations seen by the spin-lock peak at higher T, while the response of nc Li_4PS_4I would then be governed by the fluctuations sensed by the spin-lock peak appearing at lower T. Such a view might serve as an alternative explanation for the change in σ_0 and $\nu_{0,e}$ seen by macroscopic methods.

4. CONCLUSIONS

We studied the effect of local structural disorder on overall ion dynamics in Li_4PS_4I. The defect-rich nc form of the thiophosphate has been prepared by soft ball milling of the coarse-grained starting materials, which we synthesized by classical solid-state procedures. As studied by broadband conductivity spectroscopy, structural disorder leads to an increase of Li ion conductivity by almost 2 orders of magnitude, that is, it increased from 2.9×10^{-5} to 0.47×10^{-3} S cm^{-1}. This increase, which corroborates recent studies by Strauss et al.,[62,64] is accompanied by a significant decrease of the conductivity activation energy from 0.49 to 0.35 eV. The migration activation energy, as probed by electric modulus spectroscopy, changed from 0.43 to 0.29 eV. Here, we have not only determined activation energies but also tried to understand the change in apparent attempt frequencies seen in our macroscopic electrical measurements. Indeed, using the multiexcitation approach, one may rationalize a decrease of the (macroscopic) effective attempt frequency by a factor of 20. NMR relaxation, on the other hand, does not indicate a strong change in attempt frequencies.

σ_{dc} reveals a change in the conduction mechanism at $T >$ 400 K, which is also seen in ^{7}Li NMR quadrupolar spectra. Stabilization of this process down to room temperature would boost ionic conductivity at 300 K by another order of magnitude. The complex diffusion behavior in Li_4PS_4I is finally fully revealed in NMR measurements where rapid Li ion dynamics manifests as a pronounced heterogeneous motional line narrowing. Averaging and reappearance of quadrupolar intensities flanking the NMR central line clearly unveils a stepwise activation of several diffusion pathways in the thiophosphate. Time-domain NMR relaxation measurements do also mirror this behavior and point to activation energies spanning a wide range of values, that is, from 0.13 to 0.34 eV for Li ion hopping in nc Li_4PS_4I. These values characterize Li ion hopping on the various time scales to which NMR is sensitive, that is, including local [forward and backward (0.13 eV)] as well as successful displacements (0.34 eV). The latter value, which is deduced from the high-T flank of so-called spin-lock NMR relaxation measurements, determines long-range ion hopping and is in excellent agreement with that probed by electrical spectroscopy ($E_{a,M}$ = 0.29 eV, $E_{a,dc}$ = 0.35 eV). We would, however, explicitly say that in very fast ionic conductors, the traditional picture of a static barrier seems to insufficient, as has already been pointed out by Pardee and Mahan in 1975.[95] Rather, a complex interplay between the mobile species and the lattice, especially in systems with polyanions, is expected, which might be seen in NMR relaxation.[96,97]

Lastly, in conjunction with the stepwise activation of diffusion pathways, we find indications of *anisotropic* Li^+ conduction in Li_4PS_4I as evidenced by both ac impedance data and ^{7}Li NMR relaxation rates. We believe that Li^+ hopping is rather rapid along the *c*-axis and that the Li ions use the channels formed by the Li4 and Li3 positions to diffuse through the material. Since the Li5 position becomes populated at elevated temperatures, we assume that, on the NMR time scale, this site gets involved in overall Li^+ exchange processes only at higher temperatures. The latter would also be in agreement with the stepwise appearance and disappearance of the NMR electric quadrupolar satellite intensities.

■ ASSOCIATED CONTENT

Supporting Information

The Supporting Information is available free of charge at https://pubs.acs.org/doi/10.1021/acs.chemmater.3c02988.

Further ^{6}Li and ^{127}I MAS NMR spectra and additional ac conductivity isotherms of unmilled Li_4PS_4I (PDF)

■ AUTHOR INFORMATION

Corresponding Author

H. Martin R. Wilkening − *Institute of Chemistry and Technology of Materials (NAWI Graz), Graz University of Technology, Graz 8010, Austria;* orcid.org/0000-0001-9706-4892; Email: wilkening@tugraz.at

Authors

Anna Jodlbauer − *Institute of Chemistry and Technology of Materials (NAWI Graz), Graz University of Technology, Graz 8010, Austria;* orcid.org/0009-0008-6887-4106

Jonas Spychala − *Institute of Chemistry and Technology of Materials (NAWI Graz), Graz University of Technology, Graz 8010, Austria;* orcid.org/0000-0001-8315-6163

Katharina Hogrefe − *Institute of Chemistry and Technology of Materials (NAWI Graz), Graz University of Technology, Graz 8010, Austria;* orcid.org/0000-0002-2747-405X

Bernhard Gadermaier − *Institute of Chemistry and Technology of Materials (NAWI Graz), Graz University of Technology, Graz 8010, Austria;* orcid.org/0000-0003-2917-1818

Complete contact information is available at: https://pubs.acs.org/10.1021/acs.chemmater.3c02988

Author Contributions

†A.J. and J.S. contributed equally.

Notes

The authors declare no competing financial interest.

■ ACKNOWLEDGMENTS

We appreciate financial support by FFG, SFG within the SafeLIB COMET K-project. Furthermore, we thank the Deutsche Forschungsgemeinschaft (DFG) [WI3600 (4-1 and 2-1)] for additional financial support to carry out the NMR and impedance measurements.

■ REFERENCES

(1) Zhu, Z.; Jiang, T.; Ali, M.; Meng, Y.; Jin, Y.; Cui, Y.; Chen, W. Rechargeable Batteries for Grid Scale Energy Storage. *Chem. Rev.* **2022**, *122*, 16610−16751.

(2) Goodenough, J. B.; Kim, Y. Challenges for Rechargeable Li Batteries. *Chem. Mater.* **2010**, *22*, 587−603.

(3) Whittingham, M. S. Lithium Batteries and Cathode Materials. *Chem. Rev.* **2004**, *104*, 4271−4302.

(4) Brédas, J.-L.; Buriak, J. M.; Caruso, F.; Choi, K.-S.; Korgel, B. A.; Palacín, M. R.; Persson, K.; Reichmanis, E.; Schüth, F.; Seshadri, R.; Ward, M. D. An Electrifying Choice for the 2019 Chemistry Nobel

Prize: Goodenough, Whittingham, and Yoshino. *Chem. Mater.* **2019**, *31*, 8577−8581.
(5) Chen, Y.; Kang, Y.; Zhao, Y.; Wang, L.; Liu, J.; Li, Y.; Liang, Z.; He, X.; Li, X.; Tavajohi, N.; Li, B. A Review of Lithium-Ion Battery Safety Concerns: The Issues, Strategies, and Testing standards. *J. Energy Chem.* **2021**, *59*, 83−99.
(6) Janek, J.; Zeier, W. G. A Solid Future for Battery Development. *Nat. Energy* **2016**, *1*, 16141.
(7) Kato, Y.; Hori, S.; Saito, T.; Suzuki, K.; Hirayama, M.; Mitsui, A.; Yonemura, M.; Iba, H.; Kanno, R. High-Power All-Solid-State Batteries Using Sulfide Superionic Conductors. *Nat. Energy* **2016**, *1*, 16030.
(8) Birke, P.; Salam, F.; Döring, S.; Weppner, W. A First Approach to a Monolithic All Solid State Inorganic Lithium Battery. *Solid State Ionics* **1999**, *118*, 149−157.
(9) Manthiram, A.; Yu, X.; Wang, S. Lithium Battery Chemistries Enabled by Solid-State Electrolytes. *Nat. Rev. Mater.* **2017**, *2*, 16103.
(10) Bachman, J. C.; Muy, S.; Grimaud, A.; Chang, H.-H.; Pour, N.; Lux, S. F.; Paschos, O.; Maglia, F.; Lupart, S.; Lamp, P.; Giordano, L.; Shao-Horn, Y. Inorganic Solid-State Electrolytes for Lithium Batteries: Mechanisms and Properties Governing Ion Conduction. *Chem. Rev.* **2016**, *116*, 140−162.
(11) Thangadurai, V.; Narayanan, S.; Pinzaru, D. Garnet-type solid-state fast Li ion conductors for Li batteries: critical review. *Chem. Soc. Rev.* **2014**, *43*, 4714−4727.
(12) Zhang, Z.; Shao, Y.; Lotsch, B.; Hu, Y.-S.; Li, H.; Janek, J.; Nazar, L. F.; Nan, C.-W.; Maier, J.; Armand, M.; Chen, L. New Horizons for Inorganic Solid State Ion Conductors. *Energy Environ. Sci.* **2018**, *11*, 1945−1976.
(13) Ohno, S.; Banik, A.; Dewald, G. F.; Kraft, M. A.; Krauskopf, T.; Minafra, N.; Till, P.; Weiss, M.; Zeier, W. G. Materials Design of Ionic Conductors for Solid State Batteries. *Progr. Energy* **2020**, *2*, 022001.
(14) Uitz, M.; Epp, V.; Bottke, P.; Wilkening, M. Ion Dynamics in Solid Electrolytes for Lithium Batteries. *J. Electroceram.* **2017**, *38*, 142−156.
(15) Lee, Y.-G.; Fujiki, S.; Jung, C.; Suzuki, N.; Yashiro, N.; Omoda, R.; Ko, D. S.; Shiratsuchi, T.; Sugimoto, T.; Ryu, S.; Ko, J. H.; Watanabe, T.; Park, Y.; Aihara, Y.; Im, D.; Han, I. T. High-Energy Long-Cycling All-Solid-State Lithium Metal Batteries Enabled by Silver-Carbon Composite Anodes. *Nat. Energy* **2020**, *5*, 299−308.
(16) Reddy, M. V.; Julien, C. M.; Mauger, A.; Zaghib, K. Sulfide and Oxide Inorganic Solid Electrolytes for All-Solid-State Li Batteries: A Review. *Nanomaterials* **2020**, *10*, 1606.
(17) Boulineau, S.; Courty, M.; Tarascon, J.-M.; Viallet, V. Mechanochemical Synthesis of Li-argyrodite Li_6PS_5X (X = Cl, Br, I) as Sulfur-Based Solid Electrolytes for All Solid State Batteries Application. *Solid State Ionics* **2012**, *221*, 1−5.
(18) Kamaya, N.; Homma, K.; Yamakawa, Y.; Hirayama, M.; Kanno, R.; Yonemura, M.; Kamiyama, T.; Kato, Y.; Hama, S.; Kawamoto, K.; Mitsui, A. A Lithium Superionic Conductor. *Nat. Mater.* **2011**, *10*, 682−686.
(19) Deiseroth, H. J.; Kong, S. T.; Eckert, H.; Vannahme, J.; Reiner, C.; Zaiß, T.; Schlosser, M. Li_6PS_5X: A Class of Crystalline Li-Rich Solids with an Unusually High Li^+ Mobility. *Angew. Chem., Int. Ed.* **2008**, *47*, 755−758.
(20) Deiseroth, H.-J.; Kong, S.-T.; Eckert, H.; Vannahme, J.; Reiner, C.; Zaiß, T.; Schlosser, M. Li_6PS_5X: a class of crystalline Li-rich solids with an unusually high Li^+ mobility. *Angew. Chem. Inter. Ed.* **2008**, *120*, 767−770.
(21) Epp, V.; Gün, Ö.; Deiseroth, H.-J.; Wilkening, M. Highly Mobile Ions: Low-Temperature NMR Directly Probes Extremely Fast Li^+ Hopping in Argyrodite-Type Li_6PS_5Br. *J. Phys. Chem. Lett.* **2013**, *4*, 2118−2123.
(22) Hanghofer, I.; Brinek, M.; Eisbacher, S. L.; Bitschnau, B.; Volck, M.; Hennige, V.; Hanzu, I.; Rettenwander, D.; Wilkening, H. M. R. Substitutional Disorder: Structure and Ion dynamics of the Argyrodites Li_6PS_5Cl, Li_6PS_5Br and Li_6PS_5I. *Phys. Chem. Chem. Phys.* **2019**, *21*, 8489−8507.
(23) Mizuno, F.; Hayashi, A.; Tadanaga, K.; Tatsumisago, M. New, Highly Ion-Conductive Crystals Precipitated from Li_2S-P_2S_5 Glasses. *Adv. Mater.* **2005**, *17*, 918−921.
(24) Hayashi, A.; Hama, S.; Minami, T.; Tatsumisago, M. Formation of Superionic Crystals from Mechanically Milled Li_2S-P_2S_5 Glasses. *Electrochem. Commun.* **2003**, *5*, 111−114.
(25) Hayashi, A.; Hama, S.; Mizuno, F.; Tadanaga, K.; Minami, T.; Tatsumisago, M. Characterization of Li_2S-P_2S_5 Glass-Ceramics as a Solid Electrolyte for Lithium Secondary Batteries. *Solid State Ionics* **2004**, *175*, 683−686.
(26) Dietrich, C.; Weber, D. A.; Sedlmaier, S. J.; Indris, S.; Culver, S. P.; Walter, D.; Janek, J.; Zeier, W. G. Lithium Ion Conductivity in Li_2S-P_2S_5 Glasses − Building Units and Local Structure Evolution During the Crystallization of Superionic Conductors Li_3PS_4, $Li_7P_3S_{11}$ and $Li_4P_2S_7$. *J. Mater. Chem. A* **2017**, *5*, 18111−18119.
(27) Lau, J.; DeBlock, R. H.; Butts, D. M.; Ashby, D. S.; Choi, C. S.; Dunn, B. S. Sulfide Solid Electrolytes for Lithium Battery Applications. *Adv. Energy Mater.* **2018**, *8*, 1800933.
(28) Lee, H.; Oh, P.; Kim, J.; Cha, H.; Chae, S.; Lee, S.; Cho, J. Advances and Prospects of Sulfide All-Solid-State Lithium Batteries via One-to-One Comparison with Conventional Liquid Lithium Ion Batteries. *Adv. Mater.* **2019**, *31*, 1900376.
(29) Tippens, J.; Miers, J. C.; Afshar, A.; Lewis, J. A.; Cortes, F. J. Q.; Qiao, H.; Marchese, T. S.; Di Leo, C. V.; Saldana, C.; McDowell, M. T. Visualizing Chemomechanical Degradation of a Solid-State Battery Electrolyte. *ACS Energy Lett.* **2019**, *4*, 1475−1483.
(30) Zhu, Y.; He, X.; Mo, Y. Origin of Outstanding Stability in the Lithium Solid Electrolyte Materials: Insights from Thermodynamic Analyses Based on First-Principles Calculations. *ACS Appl. Mater. Interface* **2015**, *7*, 23685−23693.
(31) Schwietert, T. K.; Vasileiadis, A.; Wagemaker, M. First-Principles Prediction of the Electrochemical Stability and Reaction Mechanisms of Solid-State Electrolytes. *JACS Au* **2021**, *1*, 1488−1496.
(32) Haruyama, J.; Sodeyama, K.; Han, L.; Takada, K.; Tateyama, Y. Space−Charge Layer Effect at Interface between Oxide Cathode and Sulfide Electrolyte in All-Solid-State Lithium-Ion Battery. *Chem. Mater.* **2014**, *26*, 4248−4255.
(33) Auvergniot, J.; Cassel, A.; Ledeuil, J.-B.; Viallet, V.; Seznec, V.; Dedryvère, R. Interface Stability of Argyrodite Li_6PS_5Cl toward $LiCoO_2$, $LiNi_{1/3}Co_{1/3}Mn_{1/3}O_2$, and $LiMn_2O_4$ in Bulk All-Solid-State Batteries. *Chem. Mater.* **2017**, *29*, 3883−3890.
(34) Xiao, Y.; Wang, Y.; Bo, S.-H.; Kim, J. C.; Miara, L. J.; Ceder, G. Understanding Interface Stability in Solid-State Batteries. *Nat. Rev. Mater.* **2019**, *5*, 105−126.
(35) Bron, P.; Roling, B.; Dehnen, S. Impedance Characterization Reveals Mixed Conducting Interphases between Sulfidic Superionic Conductors and Lithium Metal Electrodes. *J. Power Sources* **2017**, *352*, 127−134.
(36) Wu, L.; Liu, G.; Wan, H.; Weng, W.; Yao, X. Superior Lithium-Stable $Li_7P_2S_8I$ Solid Electrolyte for All-Solid-State Lithium Batteries. *J. Power Sources* **2021**, *491*, 229565.
(37) Malugani, J. P.; Robert, G. Preparation and Electrical Properties of the $0.37Li_2S$-$0.18P_2S_5$-0.45LiI Glass. *Solid State Ionics* **1980**, *1*, 519−523.
(38) Mercier, R.; Malugani, J.-P.; Fahys, B.; Robert, G. Superionic Conduction in Li_2S - P_2S_5 - LiI - Glasses. *Solid State Ionics* **1981**, *5*, 663−666.
(39) Ujiie, S.; Hayashi, A.; Tatsumisago, M. Structure, Ionic Conductivity and Electrochemical Stability of Li_2S-P_2S_5-LiI Glass and Glass−Ceramic Electrolytes. *Solid State Ionics* **2012**, *211*, 42−45.
(40) Aihara, Y.; Ito, S.; Omoda, R.; Yamada, T.; Fujiki, S.; Watanabe, T.; Park, Y.; Doo, S. The Electrochemical Characteristics and Applicability of an Amorphous Sulfide-Based Solid Ion Conductor for the Next-Generation Solid-State Lithium Secondary Batteries. *Front. Energy Res.* **2016**, *4*, 18.
(41) Rangasamy, E.; Liu, Z.; Gobet, M.; Pilar, K.; Sahu, G.; Zhou, W.; Wu, H.; Greenbaum, S.; Liang, C. An Iodide-Based $Li_7P_2S_8I$ Superionic Conductor. *J. Am. Chem. Soc.* **2015**, *137*, 1384−1387.

https://doi.org/10.1021/acs.chemmater.3c02988
Chem. Mater. 2024, 36, 1648−1664

(42) Sedlmaier, S. J.; Indris, S.; Dietrich, C.; Yavuz, M.; Dräger, C.; von Seggern, F.; Sommer, H.; Janek, J. Li_4PS_4I: A Li^+ Superionic Conductor Synthesized by a Solvent-Based Soft Chemistry Approach. *Chem. Mater.* **2017**, *29*, 1830−1835.
(43) Sicolo, S.; Kalcher, C.; Sedlmaier, S. J.; Janek, J.; Albe, K. Diffusion Mechanism in the Superionic Conductor Li_4PS_4I Studied by First-Principles Calculations. *Solid State Ionics* **2018**, *319*, 83−91.
(44) Strauss, F.; Lin, J.; Karger, L.; Weber, D.; Brezesinski, T. Probing the Lithium Substructure and Ionic Conductivity of the Solid Electrolyte Li_4PS_4I. *Inorg. Chem.* **2022**, *61*, 5885−5890.
(45) Miß, V.; Neuberger, S.; Winter, E.; Weiershäuser, J. O.; Gerken, D.; Xu, Y.; Krüger, S.; di Capua, F.; Vogel, M.; Schmedt auf der Günne, J.; Roling, B. Heat Treatment-Induced Conductivity Enhancement in Sulfide-Based Solid Electrolytes: What is the Role of the Thio-LISICON II Phase and of Other Nanoscale Phases? *Chem. Mater.* **2022**, *34*, 7721−7729.
(46) Hogrefe, K.; Minafra, N.; Zeier, W. G.; Wilkening, H. M. R. Tracking Ions the Direct Way: Long-Range Li^+ Dynamics in the Thio-LISICON Family Li_4MCh_4 (M = Sn, Ge; Ch = S, Se) as Probed by ^7Li NMR Relaxometry and ^7Li Spin-Alignment Echo NMR. *J. Phys. Chem. C* **2021**, *125*, 2306−2317.
(47) Stanje, B.; Rettenwander, D.; Breuer, S.; Uitz, M.; Berendts, S.; Lerch, M.; Uecker, R.; Redhammer, G.; Hanzu, I.; Wilkening, M. Solid Electrolytes: Extremely Fast Charge Carriers in Garnet-Type $Li_6La_3ZrTaO_{12}$ Single Crystals. *Ann. Phys.* **2017**, *529*, 1700140.
(48) Morales, D. J.; Greenbaum, S. NMR Investigations of Crystalline and Glassy Solid Electrolytes for Lithium Batteries: A Brief Review. *Int. J. Mol. Sci.* **2020**, *21*, 3402.
(49) Schweiger, L.; Hogrefe, K.; Gadermaier, B.; Rupp, J. L. M.; Wilkening, H. M. R.; Wilkening, H. Ionic Conductivity of Nanocrystalline and Amorphous $Li_{10}GeP_2S_{12}$: The Detrimental Impact of Local Disorder on Ion Transport. *J. Am. Chem. Soc.* **2022**, *144*, 9597−9609.
(50) Gombotz, M.; Lunghammer, S.; Breuer, S.; Hanzu, I.; Preishuber-Pflügl, F.; Wilkening, H. M. R. Spatial Confinement − Rapid 2D F^- Diffusion in Micro- and Nanocrystalline $RbSn_2F_5$. *Phys. Chem. Chem. Phys.* **2019**, *21*, 1872−1883.
(51) Maier, J. Ionic Conduction in Space Charge Regions. *Prog. Solid State Chem.* **1995**, *23*, 171−263.
(52) Sata, N.; Eberman, K.; Eberl, K.; Maier, J. Mesoscopic Fast ion Conduction in Nanometre-Scale Planar Heterostructures. *Nature* **2000**, *408*, 946−949.
(53) Maier, J. Nanoionics: Ionic Charge Carriers in Small Systems. *Phys. Chem. Chem. Phys.* **2009**, *11*, 3011−3022.
(54) Epp, V.; Gün, Ö.; Deiseroth, H.-J.; Wilkening, M. Long-Range Li^+ Dynamics in the Lithium Argyrodite Li_7PSe_6 as Probed by Rotating-Frame Spin-Lattice Relaxation NMR. *Phys. Chem. Chem. Phys.* **2013**, *15*, 7123−7132.
(55) Köcher, S. S.; Schleker, P.; Graf, M.; Eichel, R.-A.; Reuter, K.; Granwehr, J.; Scheurer, C. Chemical Shift Reference Scale for Li Solid State NMR Derived by First-Principles DFT Calculations. *J. Magn. Reson.* **2018**, *297*, 33−41.
(56) Williamson, G. K.; Hall, W. H. X-Ray Line Broadening from Filed Aluminium and Wolfram. *Acta Metall.* **1953**, *1*, 22−31.
(57) Gombotz, M.; Wilkening, A.; Wilkening, H. M. R. Lithium Ion Transport in Micro- and Nanocrystalline Lithium Sulphide Li_2S. *Z. Naturforsch., B: J. Chem. Sci.* **2022**, *77*, 397−404.
(58) Düvel, A.; Heitjans, P.; Fedorov, P.; Scholz, G.; Cibin, G.; Chadwick, A. V.; Pickup, D. M.; Ramos, S.; Sayle, L. W. L.; Sayle, E. K. L.; Sayle, T. X. T.; Sayle, D. C. Is Geometric Frustration-Induced Disorder a Recipe for High Ionic Conductivity? *J. Am. Chem. Soc.* **2017**, *139*, 5842−5848.
(59) Gobet, M.; Greenbaum, S.; Sahu, G.; Liang, C. Structural Evolution and Li Dynamics in Nanophase Li_3PS_4 by Solid-State and Pulsed-Field Gradient NMR. *Chem. Mater.* **2014**, *26*, 3558−3564.
(60) Poudel, T. P.; Deck, M. J.; Wang, P.; Hu, Y.-Y. Transforming Li_3PS_4 Via Halide Incorporation: a Path to Improved Ionic Conductivity and Stability in All-Solid-State Batteries. *Adv. Funct. Mater.* **2023**, 2309656.
(61) Brinek, M.; Hiebl, C.; Wilkening, H. M. R. Understanding the Origin of Enhanced Li-Ion Transport in Nanocrystalline Argyrodite-Type Li_6PS_5I. *Chem. Mater.* **2020**, *32*, 4754−4766.
(62) Strauss, F.; Teo, J. H.; Janek, J.; Brezesinski, T. Investigations Into the Superionic Glass Phase of Li_4PS_4I for Improving the Stability of High-Loading All-Solid-State Batteries. *Inorg. Chem. Front.* **2020**, *7*, 3953−3960.
(63) Gadermaier, B.; Stanje, B.; Wilkening, A.; Hanzu, I.; Heitjans, P.; Wilkening, H. M. R. Glass in Two Forms: Heterogeneous Electrical Relaxation in Nanoglassy Petalite. *J. Phys. Chem. C* **2019**, *123*, 10153−10162.
(64) Strauss, F.; Lin, J.; Janek, J.; Brezesinski, T. Influence of Synthesis Parameters on Crystallization Behavior and Ionic Conductivity of the Li_4PS_4I Solid Electrolyte. *Sci. Rep.* **2021**, *11*, 14073.
(65) Murakami, M.; Shimoda, K.; Shiotani, S.; Mitsui, A.; Ohara, K.; Onodera, Y.; Arai, H.; Uchimoto, Y.; Ogumi, Z. Dynamical Origin of Ionic Conductivity for $Li_7P_3S_{11}$ Metastable Crystal As Studied by $^{6/7}Li$ and ^{31}P Solid-State NMR. *J. Phys. Chem. C* **2015**, *119*, 24248−24254.
(66) Seino, Y.; Nakagawa, M.; Senga, M.; Higuchi, H.; Takada, K.; Sasaki, T. Analysis of the Structure and Degree of Crystallisation of $70Li_2S$-$30P_2S_5$ Glass Ceramic. *J. Mater. Chem. A* **2015**, *3*, 2756−2761.
(67) Eckert, H.; Zhang, Z.; Kennedy, J. H. Structural Transformation of Non-Oxide Chalcogenide Glasses. The Short-Range Order of Lithium Sulfide (Li_2S)-Phosphorus Pentasulfide (P_2S_5) Glasses Studied by Quantitative Phosphorus-31, Lithium-6, and Lithium-7 High-Resolution Solid-State NMR. *Chem. Mater.* **1990**, *2*, 273−279.
(68) Hayashi, S.; Hayamizu, K. Accurate Determination of NMR Chemical Shifts in Alkali Halides and Their Correlation with Structural Factors. *Bull. Chem. Soc. Jpn.* **1990**, *63*, 913−919.
(69) Eckert, H.; Zhang, Z.; Kennedy, J. H. Glass Formation in Non-Oxide Chalcogenide Systems. Structural Elucidation of Li_2S-SiS_2-LiI Solid Electrolytes by Quantitative ^{29}Si, ^6Li and ^7Li High-Resolution Solid State NMR Methods. *J. Non-Cryst. Solids* **1989**, *107*, 271−282.
(70) Koch, B.; Kong, S. T.; Gün, Ö.; Deiseroth, H.-J.; Eckert, H. Site Preferences and Ion Dynamics in Lithium Chalcohalide Solid Solutions with Argyrodite Structure: I. A Multinuclear Solid State NMR Study of the System $Li_6PS_{5-x}Se_xI$ and of Li_6AsS_5I. *Z. Phys. Chem.* **2022**, *236*, 853−874.
(71) Jonscher, A. K. The 'Universal' Dielectric Response. *Nature* **1977**, *267*, 673−679.
(72) Sidebottom, D. L. Dimensionality Dependence of the Conductivity Dispersion in Ionic Materials. *Phys. Rev. Lett.* **1999**, *83*, 983−986.
(73) Irvine, J. T. S.; Sinclair, D. C.; West, A. R. Electroceramics: Characterization by Impedance Spectroscopy. *Adv. Mater.* **1990**, *2*, 132−138.
(74) Rice, M.; Roth, W. Ionic Transport in Superionic Conductors: A Theoretical Model. *J. Solid State Chem.* **1972**, *4*, 294−310.
(75) Uvarov, N. F.; Hairetdinov, E. F. The Compensation Law for Conductivity of Ionic Crystals. *J. Solid State Chem.* **1986**, *62*, 1−10.
(76) Muy, S.; Bachman, J. C.; Chang, H.-H.; Giordano, L.; Maglia, F.; Lupart, S.; Lamp, P.; Zeier, W. G.; Shao-Horn, Y. Lithium Conductivity and Meyer−Neldel Rule in Li_3PO_4-Li_3VO_4-Li_4GeO_4 Lithium Superionic Conductors. *Chem. Mater.* **2018**, *30*, 5573−5582.
(77) Bernges, T.; Hanus, R.; Wankmiller, B.; Imasato, K.; Lin, S.; Ghidiu, M.; Gerlitz, M.; Peterlechner, M.; Graham, S.; Hautier, G.; Pei, Y.; Hansen, M. R.; Wilde, G.; Snyder, G. J.; George, J.; Agne, M. T.; Zeier, W. G. Considering the Role of Ion Transport in Diffuson-Dominated Thermal Conductivity. *Adv. Energy Mater.* **2022**, *12*, 2200717.
(78) Gao, Y.; Li, N.; Wu, Y.; Yang, W.; Bo, S.-H. Rethinking the Design of Ionic Conductors Using Meyer−Neldel-Conductivity Plot. *Adv. Energy Mater.* **2021**, *11*, 2100325.
(79) Ladenstein, L.; Simic, S.; Kothleitner, G.; Rettenwander, D.; Wilkening, H. M. R. Anomalies in Bulk Ion Transport in the Solid Solutions of $Li_7La_3M_2O_{12}$ (M = Hf, Sn) and $Li_5La_3Ta_2O_{12}$. *J. Phys. Chem. C* **2020**, *124*, 16796−16805.

https://doi.org/10.1021/acs.chemmater.3c02988
Chem. Mater. 2024, 36, 1648−1664

(80) Yelon, A.; Movaghar, B.; Branz, H. M. Origin and Consequences of the Compensation (Meyer−Neldel) Law. *Phys. Rev. B: Condens. Matter Mater. Phys.* **1992**, *46*, 12244−12250.
(81) Bloembergen, N.; Purcell, E. M.; Pound, R. V. Relaxation Effects in Nuclear Magnetic Resonance Absorption. *Phys. Rev.* **1948**, *73*, 679−712.
(82) Wilkening, M.; Heitjans, P. From Micro to Macro- Access to Long-Range Li^+ Diffusion Parameters in Solids via Microscopic $^{6,7}Li$ Spin-Alignment Echo NMR Spectroscopy. *ChemPhysChem* **2012**, *13*, 53−65.
(83) Wilkening, M.; Bork, D.; Indris, S.; Heitjans, P. Diffusion in Amorphous $LiNbO_3$ Studied by ^7Li NMR − Comparison with the Nano- and Microcrystalline material. *Phys. Chem. Chem. Phys.* **2002**, *4*, 3246−3251.
(84) Wilkening, M.; Heitjans, P. Li Jump Process in *h*-$Li_{0.7}TiS_2$ Studied by Two-Time ^7Li Spin-Alignment Echo NMR and Comparison with Results on Two-Dimensional Diffusion from Nuclear Magnetic Relaxation. *Phys. Rev. B: Condens. Matter Mater. Phys.* **2008**, *77*, 024311.
(85) Bertermann, R.; Müller-Warmuth, W. Universality of NMR Results in LISICON Systems and Other Solid Lithium Conductors. *Z. fur Naturforsch. - B J. Chem. Sci.* **1998**, *53*, 863−873.
(86) Bertermann, R.; Müller-Warmuth, W.; Jansen, C.; Hiltmann, F.; Krebs, B. NMR Studies of the Lithium Dynamics in Two Thioborate Superionic Conductors: $Li_9B_{19}S_{33}$ and $Li_{4-2x}Sr_{2+x}B_{10}S_{19}$ ($x \approx 0.27$). *Solid State Ionics* **1999**, *117*, 245−255.
(87) Grüne, M.; Müller-Warmuth, W.; Hebel, P.; Krebs, B. Complex Lithium Dynamics in the Novel Thioborate $Li_5B_7S_{13}$ Revealed by NMR Relaxation and Lineshape Studies. *Solid State Ionics* **1995**, *78*, 305−313.
(88) Wilkening, M.; Epp, V.; Feldhoff, A.; Heitjans, P. Tuning the Li Diffusivity of Poor Ionic Conductors by Mechanical Treatment: High Li Conductivity of Strongly Defective $LiTaO_3$ Nanoparticles. *J. Phys. Chem. C* **2008**, *112*, 9291−9300.
(89) Zettl, R.; Gombotz, M.; Clarkson, D.; Greenbaum, S. G.; Ngene, P.; de Jongh, P. E.; Wilkening, H. M. R. Li-Ion Diffusion in Nanoconfined $LiBH_4$-LiI/Al_2O_3: From 2D Bulk Transport to 3D Long-Range Interfacial Dynamics. *ACS Appl. Mater. Interface* **2020**, *12*, 38570−38583.
(90) Breuer, S.; Uitz, M.; Wilkening, H. M. R. Rapid Li Ion Dynamics in the Interfacial Regions of Nanocrystalline Solids. *J. Phys. Chem. Lett.* **2018**, *9*, 2093−2097.
(91) Heitjans, P.; Masoud, M.; Feldhoff, A.; Wilkening, M. NMR and Impedance Studies of Nanocrystalline and Amorphous Ion Conductors: Lithium Niobate as a Model System. *Faraday Discuss.* **2007**, *134*, 67−82.
(92) Heitjans, P.; Indris, S. Diffusion and Ionic Conduction in Nanocrystalline Ceramics. *J. Phys.: Condens. Matter* **2003**, *15*, R1257.
(93) Wohlmuth, D.; Epp, V.; Wilkening, M. Fast Li Ion Dynamics in the Solid Electrolyte $Li_7P_3S_{11}$ as Probed by $^{6,7}Li$ NMR Spin-Lattice Relaxation. *ChemPhysChem* **2015**, *16*, 2582−2593.
(94) Wilkening, M.; Heitjans, P. Extremely Slow Cation Exchange Processes in Li_4SiO_4 Probed Directly by Two-Time ^7Li Stimulated-Echo Nuclear Magnetic Resonance Spectroscopy. *J. Phys.: Condens. Matter* **2006**, *18*, 9849.
(95) Pardee, W.; Mahan, G. Disorder and Ionic Polarons in Solid Electrolytes. *J. Solid State Chem.* **1975**, *15*, 310−324.
(96) Hanghofer, I.; Gadermaier, B.; Wilkening, H. M. R. Fast Rotational Dynamics in Argyrodite-Type Li_6PS_5X (X: Cl, Br, I) as Seen by ^{31}P Nuclear Magnetic Relaxation − On Cation-Anion Coupled Transport in Thiophosphates. *Chem. Mater.* **2019**, *31*, 4591−4597.
(97) Hogrefe, K.; Hanghofer, I.; Wilkening, H. M. R. With a Little Help from ^{31}P NMR: The Complete Picture on Localized and Long-Range Li^+ Diffusion in Li_6PS_5I. *J. Phys. Chem. C* **2021**, *125*, 22457−22463.

https://doi.org/10.1021/acs.chemmater.3c02988
Chem. Mater. 2024, 36, 1648−1664